



Zhang, T. and Barakos, G. (2021) High-fidelity numerical analysis and optimisation of ducted propeller aerodynamics and acoustics. *Aerospace Science and Technology*, 113, 106708. (doi: [10.1016/j.ast.2021.106708](https://doi.org/10.1016/j.ast.2021.106708))

The material cannot be used for any other purpose without further permission of the publisher and is for private use only.

There may be differences between this version and the published version. You are advised to consult the publisher's version if you wish to cite from it.

<http://eprints.gla.ac.uk/237876/>

Deposited on 31 March 2021

Enlighten – Research publications by members of the University of  
Glasgow

<http://eprints.gla.ac.uk>

# High-fidelity Numerical Analysis and Optimisation of Ducted Propeller Aerodynamics and Acoustics

T. Zhang\*, G. N. Barakos†

CFD Laboratory, School of Engineering, University of Glasgow, G12 8QQ Glasgow, UK.

**This paper presents numerical analyses of aerodynamics and aeroacoustics of ducted/un-ducted propellers based on high-fidelity CFD methods, and adjoint-based aerodynamic performance optimisation of the ducted propeller by altering the duct and blade shapes. Ducted propeller experiments by NASA are chosen for validation and used as baseline designs. High-fidelity CFD simulations are performed using the in-house solver HMB3. The aeroacoustics is analysed using the CFD solutions and in-house codes based on FW-H equations. The aerodynamic and near-/far-field acoustic benefits by ducting are shown quantitatively. An adjoint-based aerodynamic optimisation framework is also applied to the ducted propeller by altering the duct shape and the blade twist distribution. The optimisation shows improved performance for the ducted propeller over the initial design, especially at higher blade pitch. The far-field acoustic benefits of the optimised designs are also examined and are maintained after the optimisation.**

## Nomenclature

*Latin*

$C$	=	Duct Chord, $m$
$C_{F_z}$	=	Axial/Propulsion Force Coefficient, $C_{F_z} = \frac{F_z}{0.5\rho_\infty(V_\infty)^2 S_{DP}}$
$C_l$	=	Lift Coefficient, $C_l = \frac{Lift}{0.5\rho_\infty(V_\infty)^2 S_{DP}}$
$C_{M_z}$	=	Axial Moment Coefficient, $C_{M_z} = \frac{M_z}{0.5\rho_\infty(V_\infty)^2 S_{DP} C}$
$D_{DP}$	=	Duct Exit Diameter, $m$
$f_i$	=	Basis Functions
$F_z$	=	Axial/Z-Direction Force, $N$
$\mathbf{I}$	=	Objective Function
$M_z$	=	Axial/Z-Direction Moment, $Nm$
$N$	=	Number of Design Variables

---

\*PhD Student, CFD Laboratory, School of Engineering, Email: t.zhang.4@research.gla.ac.uk

†Professor, SMAIAA, MRaE, CFD Laboratory, School of Engineering, Email: George.Barakos@glasgow.ac.uk

$OSPL$  = Overall Sound Pressure Level,  $OSPL = 20 \log_{10}(\frac{p'}{p_{ref}})$   
 $P$  = Pressure,  $Pa$   
 $p'$  = Sound Pressure,  $Pa$   
 $p_{ref}$  = Acoustic Reference Pressure,  $p_{ref} = 2 \times 10^{-5}[Pa]$   
 $Q$  = Torque,  $Nm$   
 $r$  = Blade Local Span Position  
 $R$  = Blade Radius,  $m$   
 $\mathbf{R}$  = Residual Vector  
 $Re$  = Reynolds Number,  $Re = V_{tip}C/\nu_{\infty}$   
 $RPM$  = Revolutions Per Minute  
 $s$  = Local Coordinate for CST Curves  
 $S_{DP}$  = Ducted Propeller Reference Area,  $S_{DP} = CD_{DP}, m^2$   
 $T$  = Thrust,  $N$   
 $\mathbf{W}$  = Conservative Flow Variables  
 $V$  = Flow Velocity,  $m/s$

#### *Greek*

$\alpha_i$  = Design Variables  
 $\beta$  = Blade Local Pitch Angle,  $^{\circ}$   
 $\lambda$  = Adjoint Vector  
 $\mu$  = Advance Ratio,  $\mu = \frac{V_{\infty}}{V_{tip}}$   
 $\nu$  = Kinematic Viscosity,  $m^2/s$   
 $\eta$  = Froude Efficiency,  $\eta = \frac{TV_{\infty}}{Q\Omega}$   
 $\Omega$  = Rotational Speed,  $rad/s$   
 $\xi$  = Local Coordinate for CST Curves

#### *Subscripts and superscripts*

$\infty, inf$  = Free-stream Value  
 $DP$  = Ducted Propeller  
 $OP$  = Open Propeller  
 $tip$  = Blade Tip Value

## *Acronyms*

CFD	=	Computational Fluid Dynamics
CST	=	Class Shape Transformation
FW-H	=	Ffowcs Williams-Hawkings
GCI	=	Grid Convergence Index
HMB3	=	Helicopter Multi-Block 3
MRF	=	Multiple Reference Frame
NASA	=	National Aeronautics and Space Administration
SST	=	Shear Stress Transport
RANS	=	Reynolds Averaged Navier Stokes

## **I. Introduction**

In recent years, a surge in Urban Aerial Mobility (UAM) research and development can be seen around the world [1], featuring novel aircraft configurations and Electrical Vertical Take-Off and Landing (eVTOL). The UAM concept has been hailed as the next revolution in aviation, yet significant efforts are needed to form a solid, scientific foundation for design, manufacturing, operations etc. Specifically, the future UAM should be both environment- and community-friendly, while maintaining excellent aerodynamic performance especially at low speeds or hover. There are further demands for low carbon/nitrogen and noise emissions, as well as, high safety capacity and less intrusive aircraft wake, since the UAMs will operate mostly in the urban environments. As a core component of aerial vehicles, the choice and optimal design of a propulsor thus becomes the key topic to be settled.

The ducted propeller can be a very promising choice of propulsion for future UAMs. The ducted propeller, or shrouded fan/rotor, is a propeller enclosed in an annular duct with aerofoil-like sections. The presence of the duct alters significantly the inflow conditions of the propeller, thereby altering its performance. The ducted propeller is often more efficient at low speeds, especially in hover, over the un-ducted counter-part. Tests also showed acoustic reductions due to the duct shielding, while maintaining high efficiency. The duct also provides a base for further noise reduction using absorbing lining. Also, due to the expansion at the duct diffuser, the propulsor wake is less intrusive[2–4]. Moreover, by shielding the propeller, the duct provides protection to ground personnel and equipment. In emergencies, the duct can be used as containment, preventing further damage to the airframe. By adding guide vanes at the duct exit deflecting the flow, vectorized thrust can be derived and used for sideways propulsion or control. It is also ideal to make the ducted propeller an integrated, compact, electricity-driven, plug-and-play propulsor unit for future aerial vehicles. These features make the ducted propeller an ideal choice of propulsion for future UAMs operating in urban environments. A detailed review of ducted propeller research, including experiments, numerical simulations/optimisation, and research

challenges, can be found in Reference [3]. Detailed numerical analyses of the ducted propeller performance at various advance ratios, pitch settings, and cross-wind angles are also carried out by the authors in previous studies [2].

Apart from marine[5] and wind energy [6] applications, the ducted propeller has been employed by several early and modern aircraft designs. During the 1950s and 1960s, the ducted propeller was extensively tested by NASA [7] [8][9], and 2 tilt-duct prototypes, i.e. the Bell X22 and the Doak VZ4D, were built. Many of these tests employed large- or real-scale ducted propeller models, and were well documented. Recent experimental studies mostly focused on small-scale models for Unmanned/Micro Aerial Vehicle (UAV/MAV) applications. Although remain aerodynamically representative to some extent, the recent small-scale tests are not favourable if directly applied to aeronautical applications, due to the low Reynolds numbers and insignificant compressibility effects. Moreover, few modern tests publicised their detailed geometry definitions due to commercial restrictions. Regardless, most tests concluded the superior efficiency of the ducted propeller at lower advance ratios or in hover. The ducted propeller is off-loaded, while the extra thrust comes from the duct surface (at times more than 50% of the total thrust). Acoustics tests [10][11] also confirmed noise reductions due to the duct shielding. The acoustic patterns and directivities are also significantly altered due to the duct presence, yet fewer experiments continued to explore in this respect. Despite all the promising benefits discussed above, the ducted propeller is found not efficient comparing to the un-ducted propeller at higher advance ratios. Overall, due to the geometry of the duct and the blade rotation, it is hard to experimentally measure the flow details inside or in close proximity to the duct. Most tests are therefore only able to provide balance data or flow measurements outside the duct, and hence lack insight of the detailed flow physics. Such difficulties highlight the need for theoretical or numerical methods.

Theoretical studies and lower-order modelling of ducted propellers based on e.g. lifting line, blade element, and panel methods can be dated back to decades ago. Kriebel and Mendenhall [12] performed theoretical analyses for fans inside ducts. Comparisons were made against experimental data, but in many cases only qualitative agreement could be achieved. Drela et.al [13, 14] presented an open-source code DFDC (Ducted Fan Design Code) based on extensions of classic lifting line theory and panel methods. Previous tests and comparisons [2] show that the code is capable of accurate and rapid thrust predictions for ducted propellers in axial flight, but the torque is generally highly overpredicted. More recently, Bontempo and Manna [15] presented exact solutions of incompressible, axisymmetric and inviscid flow through the duct through a non-uniform actuator disk. Overall, the theoretical and lower-order predications can give rapid analyses of ducted propeller performance and is suitable for preliminary designs. However, the accuracy often suffers from incompressible, axisymmetric, and inviscid assumptions, and the propeller is often represented by actuator disks. Cross-wind conditions can hardly be accounted for due to the complex flow features.

Comparing to simplified theoretical or lower-order modelling, 3-dimensional Computational Fluid Dynamics (CFD) analyses are hence more favourable for more accurate and complex analyses of ducted propeller flow fields. In recent years, Unsteady Reynolds Averaged Navier-Stokes (URANS) simulations were carried out by Jimenez and Singh et.al.

[16] and by Biava and Barakos [17]. Detached Eddy Simulations (DES) and Delayed Detached Eddy Simulations (DDES) were attempted by Sheng et.al. [18] and Rubio et.al.[19]. Zhang and Barakos later [2] carried out extensive RANS/URANS simulations on the test case by Grunwald and Goodson [8]. Very favourable agreement with test data was noted, and large variations of operating conditions were investigated. Regardless, due to geometries, relative motions, and complex flow features, the high-fidelity CFD modelling of ducted propellers with blades resolved at various conditions remains challenging. Moreover, many simulations were performed on small-scale geometries for UAV/MAV applications, and most numerical cases lacked the support from experiments. Particularly, few to none numerical simulations attempted to investigate the acoustics in the near and far fields, due to the complexity, limitations of simulation resolutions, and again the lack of support from relevant experiments.

While many simulations focused on validation and performance examination, CFD-based design optimisation, especially for performance improvement at higher advance ratios, is necessary. However, due to restrictions of computational costs and complexity, many optimisation studies [20, 21] adopted simplified models for the propeller disk. Through this approach, the mutual interactions between the blade and the duct are not resolved in detail. Optimisation studies of the ducted propeller with resolved blades involved are rarely seen. As mentioned earlier, Biava and Barakos [17] applied RANS/URANS methods to the analysis of the ducted propulsor for Hybrid Air Vehicles. Gradient-based optimisation of the duct diffuser shape and the blade twist was attempted with adjoint formulations, and moderate improvement of the efficiency was achieved. The numerical study was supported by corresponding experiments. However, due to the proprietary nature, the geometry and the performance were not discussed in detail. Acoustic performance of the original and optimised design was also not investigated.

The objectives of this work are to quantitatively study the near-/far-field acoustic performance of the ducted propeller comparing to the open propeller counterpart, and to investigate the aerodynamic performance optimisation by altering the duct and blade shapes upon adjoint methods. High-fidelity CFD methods are adopted for accurate predictions of aerodynamic performance and for high resolution of the near-field acoustics. The near-field acoustics of the ducted/un-ducted propeller is directly extracted from the CFD solution. The far-field acoustics is calculated using the Ffowcs Williams-Hawkings (FW-H) equation[22], taking the CFD solution as input. The sensitivity-based aerodynamic optimisation study is driven by the adjoint method, for its compatibility with CFD methods and its efficient handling of many design variables. The purpose of the current optimisation study is to first demonstrate the effectiveness and efficiency of the employed method. Another goal is to explore the impact of the duct shape and blade twist variations on the aerodynamic and acoustic performance at high advance ratios.

The contents of the present paper are organised as follows. Section II presents the numerical methods employed in the present study for the CFD simulation, the near- and far-field acoustics calculation, and the adjoint-based optimisation. Section III presents a brief discussion of the validation and aerodynamic performance of a ducted propeller test case [8] by NASA. Comparisons are also made with the un-ducted counterpart. Analyses of the near-/far-field acoustics of both

configurations are also presented in this section, and acoustic benefits by ducts are shown clearly. Section IV presents an optimisation study, and performance improvements by the optimisation are analysed and examined at various advance ratios and pitch settings. The corresponding acoustics of the optimal designs are also calculated and analysed. Last but not least, conclusions derived from the current study are summarised in Section V.

## II. Numerical Methods

### A. Helicopter Multi-Block 3 (HMB3) Solver and Adjoint methods

#### *HMB3 Flow Solver*

High-fidelity CFD methods are used in the present for the accurate prediction of ducted/un-ducted propeller aerodynamic performance and for the fine resolution of the near-field flowfields for further acoustic studies. The in-house Helicopter Multi-Block (HMB3) [23, 24] CFD code is used in the present work. The code has been widely used in simulations of rotorcraft flows [25–28]. HMB3 solves the Unsteady Reynolds Averaged Navier-Stokes (URANS) equations in integral form using the Arbitrary Lagrangian Eulerian (ALE) formulation for time-dependent domains, which may include moving boundaries. The Navier-Stokes equations are discretized using a cell-centered finite volume approach on a multi-block, structured grid:

$$\frac{d}{dt} (\mathbf{W}_{i,j,k} V_{i,j,k}) = -\mathbf{R}_{i,j,k} (\mathbf{W}_{i,j,k}), \quad (1)$$

where  $i,j,k$  represent the cell index,  $\mathbf{W}$  and  $\mathbf{R}$  are the vector of conservative flow variables and residual respectively, and  $V_{i,j,k}$  is the volume of the cell  $i,j,k$ . To evaluate the convective fluxes, Osher approximate Riemman solver is used, while the viscous terms are discretized using a second order central difference scheme. The  $3^{rd}$  order MUSCL (Monotone Upstream-centered Schemes for Conservation Laws) approach is used to provide high-order accuracy in space. The chimera/overset grid method [29] is extensively used in this work. In the present work, simulations are performed with the  $k - \omega$  SST [30] turbulence model.

The Rotating Reference Frame (RRF) method is also implemented in HMB3 [17] for simulations with rotational periodicity, such as rotors in hover or axial flight. The governing flow equations are reformulated and solved in a non-inertial rotating reference frame, which transforms the unsteady problem into steady calculations. Besides reducing the computational cost, the RRF implementation is also vital for the adjoint formulation providing the flow sensitivities. With the help of periodic boundaries, the computational cost can be further reduced since only a fraction of the entire computational domain is needed. Specially, for the simulation of ducted propellers as in this work, the stationary walls, e.g. the duct surfaces, are accounted for by imposing opposite motions in the rotating frame.

#### *HMB3 Adjoint Solver*

The adjoint method[31][24], which is known for its efficient handling of large numbers of design variables with few objective functions, is adopted in the current work for the optimisation study of the ducted propeller. The current optimisation study involves many design variables governing the duct and blade shapes, with just a few objective/constraint functions e.g. the overall thrust and torque. The core of many gradient-based optimisation problems, as also involved in this work, is to solve the sensitivity equation of objective functions with respect to design variables. For aerodynamic performance optimisation using CFD methods, a typical objective function  $I$  can be explicitly defined in Equation 2:

$$I = I(\mathbf{W}(\alpha), \alpha). \quad (2)$$

where  $\alpha$  is the design variable vector, which often defines the geometry and includes dozens of parameters. Typically,  $I$  is a collection of aerodynamic loads or their combinations. Hence, it is also relying on  $\mathbf{W}(\alpha)$ , which is the conservative flow variable vector as in Equation 1. Instead of being independent variables,  $\mathbf{W}$  is now subject to design variables  $\alpha$ . The steady state residual vector  $\mathbf{R}$  of the governing flow equations, as similarly discretised in Equation 1, can now be written as:

$$\mathbf{R}(\mathbf{W}(\alpha), \alpha) = \mathbf{0}. \quad (3)$$

To evaluate changes of  $I$  with respect to variations of design variables  $\alpha$ , it is necessary to solve the sensitivity equation of  $I$  relative to  $\alpha$ . The computational requirement is large if using direct differentiation or finite differences because of the large amount of design variables. By introducing an adjoint vector  $\lambda$  correlating Equations 2 and 3, the sensitivity equation can be recast in the adjoint form as :

$$\left(\frac{\partial \mathbf{R}}{\partial \mathbf{W}}\right)^T \lambda = -\left(\frac{\partial I}{\partial \mathbf{W}}\right)^T. \quad (4)$$

$$\frac{dI}{d\alpha} = \frac{\partial I}{\partial \alpha} + \lambda^T \frac{\partial \mathbf{R}}{\partial \alpha}. \quad (5)$$

The major effort to solve the sensitivity equation 5 aligns with solving the adjoint vector  $\lambda$  coupled in the linear system in Equation 4. Given specified governing flow equations, this linear system scales only with the number of objectives  $I$  and is irrelevant to the number of design variables. In this light, the adjoint formulation is especially suitable for optimisation problems involving many design variables. Details of the HMB3 adjoint formulations can be found in previous optimisation studies of rotors, wings, and ducted propellers [24][17].

For aerodynamic performance optimisation, the input design variables usually govern shapes of wall surfaces in the CFD simulations and mesh deformation is hence involved. To adapt volumetric cells to the surface deformation, an advanced mesh deformation algorithm is implemented in HMB3 based on Inverse Distance Weighting (IDW) [32]

interpolations. The mesh deformer takes as samples the deformation of surface mesh points and calculates displacements of volumetric mesh points using the IDW interpolation. The HMB3 mesh deformer has also been successfully deployed in previous studies of aeroelastics [33] and optimisation [17].

## **B. Acoustic Calculations Methods based on CFD Results**

### *Near-field Acoustics*

In the present study, the near-field acoustics is directly derived from pressure fields resolved with high-fidelity HMB3 simulations. The sound pressure signal is extracted by subtracting the time-averaged pressure field. **This direct approach includes all acoustic sources in the near-field, subject to the near-field CFD resolution.** The similar approach can be seen used in propeller acoustic analyses using HMB3 [34]. This approach requires high-order schemes and fine spatial/temporal resolution. For the current acoustic study of the ducted propeller, the 3rd-order MUSCL scheme as described in previous sections is used. The background grid is carefully tuned to guarantee at least 10 mesh points for the wave length targeting at 4 times the BPF(1600 Hz), in the near-field region within four duct chords from the centre of rotation. Further, most acoustic analyses are made at receiver points 2 duct chords away. Additionally, as discussed earlier, the ducted propeller simulations are performed in a non-inertial, rotating reference frame as steady state. Fine temporal resolution is hence guaranteed by strong convergence of the steady calculations.

### *Far-field Acoustics*

In the present work, the far-field acoustics is efficiently calculated using the FW-H equation [22], following the Farassat Formulation 1A [35], taking as input CFD solutions of the surface pressure fields. The formulation has been widely used for far-field noise predictions of aircraft, wind turbines[36], and propellers[37]. The Farassat Formulation 1A [35] solves surface terms of the FW-H equation, i.e. the thickness noise and the loading noise, in the time domain, by introducing the retarded time concept. The formulation results in two linear equations respectively for the thickness and loading components.

The current far-field acoustic approach has ignored the quadrupole source which requires expensive integrations over volumes. This approach is reasonable considering the subsonic nature of the current study, and is efficient and sufficiently accurate for purposes of engineering analysis based on CFD results. Similar approaches were adopted for noises predictions by Luo et.al. [38] for ducted axial fans and by Dighe et.al. [36] for ducted wind turbines. Additionally, the current implementation is an extension of the existing acoustic code HFWH (Helicopter Ffows Williams-Hawkings)[37] in the high-level Julia language. Extensive code-to-code comparisons have been performed in order to verify the current implementation.

### C. Adjoint-based Optimisation Method

The proposed optimisation framework is described in the flow chart Figure 1. This framework consists of separate tools such as the flow solver, the optimiser, binaries for the mapping between the design space and the geometry, and auxiliary utilities for file I/O and system operations. Each individual tool can be substituted with new methods or implementations, such that the versatility and flexibility of the framework are ensured.

In the current work, objective and constraint functions, as well as, their derivatives with respect to design variables are calculated through the HMB3 adjoint solver. **The aerodynamic shapes are parametrised and represented by a set of design variables such as in Figure 2.** Once initial HMB3 solutions of the baseline design are checked, the optimiser is initialised and the optimisation loops begin. The optimiser yields new design variables in each iteration, upon input objectives, constraint, and derivatives from previous HMB3 solutions. The sensitivity data is required only occasionally upon the optimiser decision, hence the adjoint computation is not also triggered in every iteration. The new design variables are translated into mesh deformation **with respect to the baseline shapes**, and are fed to new HMB3 calculations. **New calculations are restarted from previous solutions for faster convergence. An efficient, inverse-distance mesh deformer[24][17] in the HMB3 solver handles the mesh deformation.** The optimisation loops stop and output a final set of design variables when set criteria are met, e.g. derivatives are approaching zero or upper limits of iterations are met etc. Shell scripts and in-house codes are composed to automate the procedures. **Comparing to meta-model-based optimisation which often requires hundreds of function evaluations, the proposed adjoint-based framework is much more efficient and delivers improved designs subject to constraints at the cost of typically just 10 to 15 CFD/adjoint evaluations.**

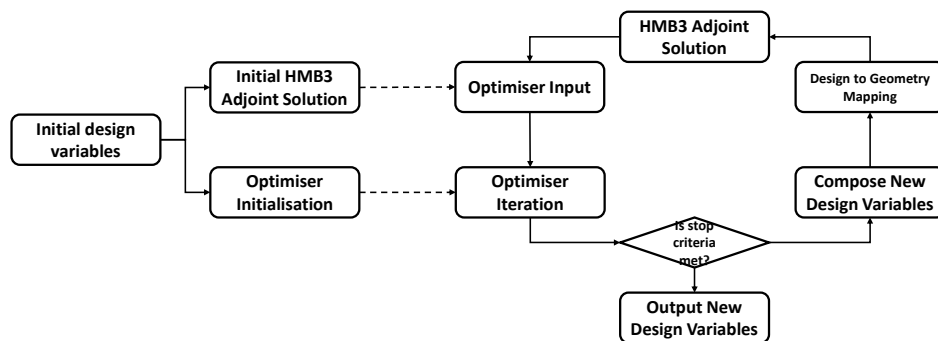


**Fig. 1 Flow chart of the duct shape optimisation.**

#### *Definition and Solution of the Non-linear Optimisation Problem*

The general form and solution methods of the non-linear optimisation problem in the present study are presented in this section. The general formulation of the non-linear optimisation involved can be written as:

$$\begin{aligned}
& \textit{Find} : \\
& \min(I(\alpha)), \\
& \textit{subject.to.} \\
& \alpha_{i,\min} \leq \alpha_i \leq \alpha_{i,\max}, i \in 1, \dots, n, \\
& g_j(\alpha) \leq 0, j \in 1, \dots, m, \\
& h_k(\alpha) = 0, k \in 1, \dots, p.
\end{aligned} \tag{6}$$

where  $I(\alpha)$  is the objective function to be minimised, subject to  $m$  inequality constraints  $g_j(\alpha)$  and  $p$  equality constraints  $h_k(\alpha)$ .  $\alpha = (\alpha_1, \dots, \alpha_n)$  is the design variable vector, of  $n$  dimensions. Specifically, the objective and constraint functions in this work are usually the thrust, torque, or their combinations, which are inherently non-linear functions of the design and flow variables.

The optimisation problem in Equation 6 is solved using a Sequential Least-Square Quadratic Programming(SLSQP) algorithm[39] as provided in the *NLopt* library [40]. The algorithm represents and minimises the objective function with successive quadratic/least-square models, while the constraints are approximated by first-order models. Nevertheless, the optimiser is programmed as a separate tool in the optimisation framework, interfaced with files.

#### *Duct Shape Parametrisation*

As has been presented in previous studies [2], for an axisymmetric ducted propeller, **the thrust augmentation mostly comes from the combination of the leading-edge suction and recovered pressures at the diffuser exit.** The mid-chord part of the duct usually plays a relatively modest role in thrust contribution and is often composed by straight lines in real-world designs [8] [9]. The mid-chord was hence fixed in the current work to exclude varying blade tip gaps and duct thickness. This is also due to the consideration that the duct thickness is often constrained by the structure or volume in practice. In this light, the parametrisation and deformation of duct shapes in this work takes into account the leading-edge and trailing-edge curves, as presented in Figure 2. Nevertheless, the deforming curve region can be extended to include most of the middle chord.

The proposed parametrisation allows a comprehensive set of variations of duct chord length, camber, inlet lip radius, and inlet/outlet expansion ratios, i.e. most geometric parameters governing the ducted propeller performance. The design variables are the parameters governing the curve shape, as well as, offsets of the leading/trailing edge points with respect to original positions. Comparing to other popular parametrisation methods such as Free Form Deformation, the proposed parametrisation approach is strongly physics-based and focuses on a smaller but more relevant design space.

This duct shape parametrisation problem can be simplified as the parametrisation of 4 curve segments, i.e. the

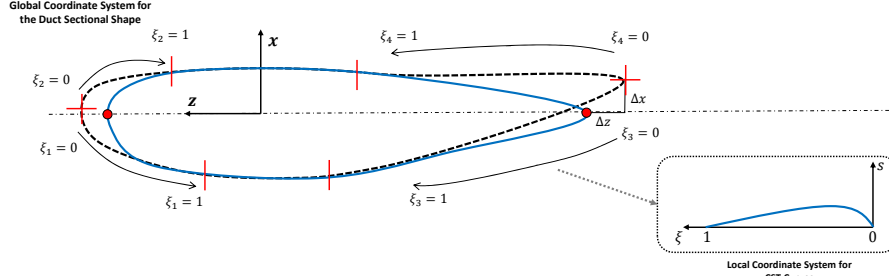


**Fig. 2 Illustration of duct shape parametrisation and deformation.**

inner leading edge, the outer leading edge, the inner trailing edge, and the outer trailing edge. The curves are locally represented by the classic CST (Class Shape Transformation) method[41] which is often used in aerofoil parametrisation. The local coordinate system for CST parametrisation is also illustrated in Figure 2.

This system is used for the CST representation of curve shapes. The horizontal axis  $\xi$  denotes the chord-wise direction, with  $\xi = 0.0$  at the starting point(leading edge) and  $\xi = 1.0$  at the ending point(sharp trailing edge). The vertical axis  $s$  is norm to chord.  $s$  can be written as a function of  $\xi$  if using classic CST representations:

$$s = CST(\xi, \alpha_i), \quad (7)$$

where  $CST(\xi, \alpha_i)$  is a generalised CST function subject to a set of coefficients  $\alpha_i$ . This coefficient array is recognised as part of the design variables. Specifically, the Bernstein basis functions were used in the current study. To enforce a rounded shape at the starting point, the  $N1$  value is set as 0.5 with  $N2 = 1.0$ .

The CST curves are later mapped back to the original global system using coordinates of curve starting and ending points. The mapping is performed linearly using equations below:

$$z = (1 - \xi)(z_0 + \Delta z) + \xi z_1, \quad (8)$$

$$x = s(\xi, \alpha_i) + (1 - \xi)(x_0 + \Delta x) + \xi x_1, \quad (9)$$

where  $(x_0 + \Delta x, z_0 + \Delta z)$  and  $(x_1, z_1)$  are global coordinates of the starting and ending points, respectively.  $\Delta x$  and  $\Delta z$  are the offset of the starting point, which are taken as design variables. This mapping method is universal for both duct leading edge and trailing edge curve segments.

### Blade Twist Parametrisation

For a ducted propeller, typically the blades face higher inflow velocities due to duct induction. It's therefore of interest to investigate blade pitch and twist variations and optimisation while changing the duct shape or axial velocities.

The current parametrisation of the blade twist is based on polynomial approximations of pitch distributions along the radial direction. The pitch distribution is represented by the following equation:

$$\beta(r_0) = \sum_{i=1}^N \alpha_i f_i r_0, \quad (10)$$

where  $r_0 = r/R$  is the non-dimensional radius,  $f_i$  is the basis function (in the current case Bernstein polynomials were used),  $\alpha_i$  are coefficients recognised as design variables, and  $N$  is the number of coefficients. Note that the proposed parametrisation describes the attack angle distribution of local blade elements along the radial direction, and therefore includes variations of the blade pitch. Through this parametrisation, the optimisation framework will deliver not only the optimal twist distribution but also the optimal pitch setting for a specific objective

### III. Aerodynamics/Aeroacoustics of Baseline Design

A ducted propeller test case by NASA[8] in the 1960s was chosen as the validation case and CFD simulations of the ducted/un-ducted propellers in axial flight were performed using the HMB3 solver. The case was chosen for its detailed geometry and test information. In addition, the ducted propeller model tested was a 5/16-scaled model of the real-world design that was used on the Doak VZ4D tilt-duct aircraft, but with a different propeller design with 3 blades. Regardless, considering the age of these experiments, some uncertainty in the geometry, and test data is expected. The duct geometry is presented in Figures 3. Note the centre-body was approximated for the simulations since no detailed information was given in the tests[8]. Details of blade shape can be found in Refs [8] and [2].

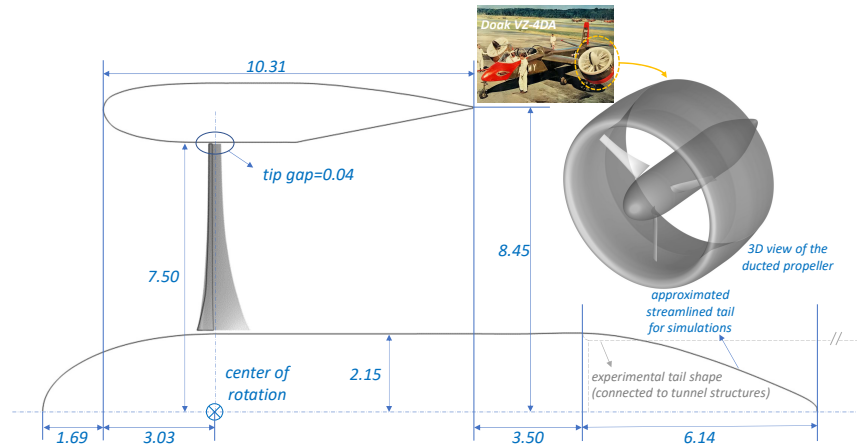


**Fig. 3 Key parameters of the Grunwald ducted propeller. Dimensions are in inches. Details of the duct shape can be found in Ref [8]. Note the center-body tail is sealed with a streamlined shape, where as in the experiments it is connected to tunnel structures.**

The simulations were performed in the Rotating Reference Frame (RRF) with periodic boundaries, hence only 1/3

of the entire physical domain was needed. The simulations were performed using steady RANS equations closed with the  $k - \omega SST$  model and were considered as fully turbulent. The grids of the components, i.e. the blade, centre-body, and the duct, and the background were generated separately and assembled for simulations using Chimera methods. The chimera grid topology used in previous studies [2] was exploited here. The simulations used the duct chord length as the reference length and the blade tip speed as the reference speed. This resulted in a Reynolds number of about  $2.8 \times 10^6$ . Initial simulations were also carried out using different reference values, e.g. the blade tip chord and the free-stream velocity, but only minor differences were noted in the performance predictions. The very small tip gap (0.04 inches) between the blade tip and duct surface, which often has a strong effect on the overall performance, was filled with 112 cells along the blade chord, 64 cells along the blade thickness, and about 65 cells along the radial directions. The first cell of the boundary layer mesh is kept below  $1 \times 10^{-5}$  of the reference length with the maximum  $y^+$  below 4, as more grid points were directed to the buffer layer. A cylindrical background grid, with uniform node distribution along the azimuthal direction, was used. Grid nodes were clustered in regions where the near-field grids reside in the axial and radial directions. Since acoustic calculations were later involved, at least 10 points were guaranteed for the acoustic wave length at 4 times the Blade Passing Frequency (BPF) within the radius of 4 duct chords from the centre of blade rotation in the background grid.

#### A. Validation and Aerodynamic Performance of Ducted/Un-ducted Propellers

A grid convergence was performed for simulations of the ducted propeller in axial flight at  $\mu = 0.191$ . The grid convergence was carried out by progressively and systematically varying the near-field grids, i.e. the duct, the centre-body, and the blade. The far-field grid, however, was always the finest and kept constant. This was to guarantee enough interpolation cells for the near-field grids, as well as, to ensure the similar amount of computational cells after the hole cutting of the chimera method. Detailed cell numbers of the grids of 3 sizes and 2 refinement levels are listed in Table 1. The resultant grid refinement ratio in the near field was about 1.25, which means the cell numbers were doubled through each refinement level. For the total grid the ratio was lower at about 1.08, due to large cell numbers in the background grid. The Grid Convergence Index (GCI) and the GCI ratios, as proposed by [42], were calculated using the Froude efficiency values in order to quantify the convergence. As suggested by Roache [43], the calculations do not necessarily depend on specific refinement ratios (2, 4, 8...), as long as the refinement ratios are greater than 1 and are almost constant. The GCI values calculated are presented in Table 2, using cell size definitions by both near-field and total cell numbers. The cell size  $h$  was represented by  $h = (N_{cell})^{-1/3}$ , where  $N_{cell}$  is the number of cells in the grid.

As can be noted in Table 2, the GCI values, calculated using both near-field and total grids, are small and are decreasing with refined grids. The GCI ratio values are very close to 1.0, indicating that the convergence is in the asymptotic region. The Richardson extrapolation [42] based on Froude efficiency results from the 3 at infinitely small

**Table 1** Details of the Chimera grids used for ducted fan simulations in axial flight (in million cells).

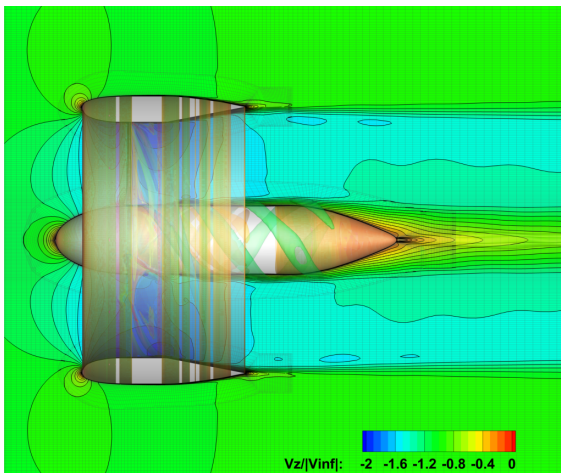
	Blade	Centre-body	Duct	Near-field Total	Background	Total
Coarse	1.33	0.243	0.385	1.958	8.72	10.678
Medium	2.13	0.513	0.77	3.413	8.72	12.133
Fine	4	1.27	1.54	6.81	8.72	15.53

**Table 2** Grid convergence study for simulations of the ducted propeller in axial flight at  $\mu = 0.191$ .

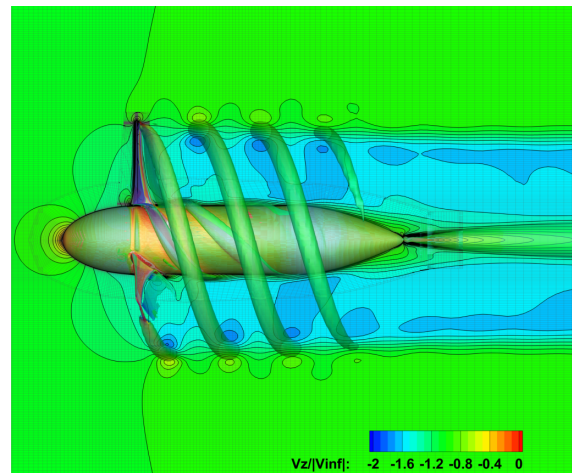
	Near-field			Total		
	Refinement Ratio	Grid Convergence Index (GCI)	GCI Ratio	Refinement Ratio	Grid Convergence Index (GCI)	GCI Ratio
Coarse-Medium	1.20	2.80E-03	99.82%	1.04	2.40E-03	99.82%
Medium-Fine	1.26	5.00E-04		1.08	1.00E-04	

cell size is very close to the fine grid result, with a relative error within 0.5%.

Flow-fields of the ducted/un-ducted propellers at  $\mu = 0.191$  in axial flight with the finest grids are shown in Figures 4(a) and 4(b). The tip vortices are visualised using iso-surfaces of dimensionless  $q$ -criterion of 0.5. The axial velocity  $V_z$  is normalised by the free-stream velocity. The ducted propeller is shown to produce weaker tip vortices and the wake is slower and smoother, comparing to the un-ducted counterpart at this axial speed. This is due to the duct diffuser that expands and slows down the exit flow, recovering the kinetic energy to pressure energy. These result in higher duct thrust, as well as, less intrusive wake to the environment, which is particularly favourable for operations near communities.



(a) Ducted propeller wake and axial velocity contours. The axial velocity  $V_z$  is normalised by the free-stream velocity.



(b) Open propeller wake and axial velocity contours. The axial velocity  $V_z$  is normalised by the free-stream velocity.

**Fig. 4** Flow-fields of the ducted/un-ducted propellers at  $\mu = 0.191$  in axial flight with the finest grids. The tip vortices are denoted by iso-surfaces of dimensionless  $q$ -criterion of 0.5.

The breakdown of aerodynamic loads of the ducted/un-ducted propellers and comparisons with experimental data at

$\mu = 0.191$ , using the finest grids in Table 1, are presented in Table 3. As seen in Table 3, comparing to the experimental data, the total thrust of the ducted propeller was very slightly under-predicted by the CFD simulations by about 3%, while the propeller torque was slightly over-predicted by about 6%. The thrust distribution over the propeller and the duct was well predicted, with the duct and centre-body carrying about 30% of the total propulsion at this advance ratio. Such agreement is favourable given the uncertainties in the geometry and the test data. After all, the experiments [8] were conducted in the 1960s and the centre-body shape was approximated in the simulations as no accurate definition was given. Simulations were also performed on the un-ducted propeller at the same  $\mu = 0.191$  on the fine grids with the duct removed for comparison purposes. Predictions suggested that the un-ducted propeller, at the same advance ratio, blade pitch and **rotating rate**, produces slightly lower total thrust and higher propeller torque, hence the Froude efficiency is lower than the ducted propeller by about 0.1. Unfortunately, no experimental data is available for the open propeller performance validation. More detailed validation of the ducted/un-ducted propellers, including lower-order predictions and variable conditions e.g. advance ratios, pitch settings, and cross-wind angles, can be found in the previous study by Zhang and Barakos [2].

**Table 3 Aerodynamic loading breakdown of the ducted/un-ducted propellers with fine grids and comparisons with experimental data [8].**

	Experiment			HMB3 Ducted Propeller				HMB3 Open Propeller	
	$F_z$ /[N]	$C_{F_z}$ /[-]	Contribution	$F_z$ /[N]	$C_{F_z}$ /[-]	Contribution	Relative Error	$F_z$ /[N]	$C_{F_z}$ /[-]
Total Thrust	89.55	1.40	100%	86.85	1.36	100%	-3%	81.67	1.28
Propeller Thrust	63.97	1.00	71%	61.27	0.96	71%	-4%	85.20	1.33
Duct(& Centre-body) Thrust	25.59	0.40	29%	25.58	0.40	29%	0%	-3.54	-0.06
Propeller Torque ( $M_z$ /[Nm], $C_{M_z}$ /[-])	4.52	0.27	-	4.79	0.29	-	6%	5.14	0.31
Froude Efficiency $\eta$ /[-]	0.70	-	-	0.66	-	-	-5%	0.58	-

More detailed performance analyses of the ducted/un-ducted propellers at various operating conditions can also be found in the previous study[2], hence only brief discussions are presented here. As also shown in Table 3, the duct surface is an important source of thrust carrying about 30% of the total propulsion, while the propeller enclosed is offloaded. Regardless, the ducted and un-ducted propellers produce similar amounts of thrust, at this advance ratio of  $\mu = 0.191$  (which was the highest advance ratios during experiments[8]). With the same pitch and **rotating rate**, beyond this advance ratio, the un-ducted propeller produces higher thrust and becomes more efficient, due to the increasing duct drag at high advance ratios. Previous investigations on pitch variations[2], using both high-fidelity CFD simulations and lower-order methods, also suggest that increasing the blade pitch causes the efficiency to drop in both ducted/un-ducted cases, and the current blade pitch setting of  $\beta_{0.75} = 29.58^\circ$  offers peak efficiencies for both cases at this advance ratio. These suggest the need for optimisation of the blade and duct geometries if higher thrust and efficiency are to be derived

from the ducted propeller at high advance ratios. However, the current baseline results at  $\mu = 0.191$  are ideal for acoustic comparisons between the ducted/un-ducted configurations, since the aerodynamic loadings are similar in this condition.

## B. Aeroacoustics of Ducted/Un-ducted Propellers

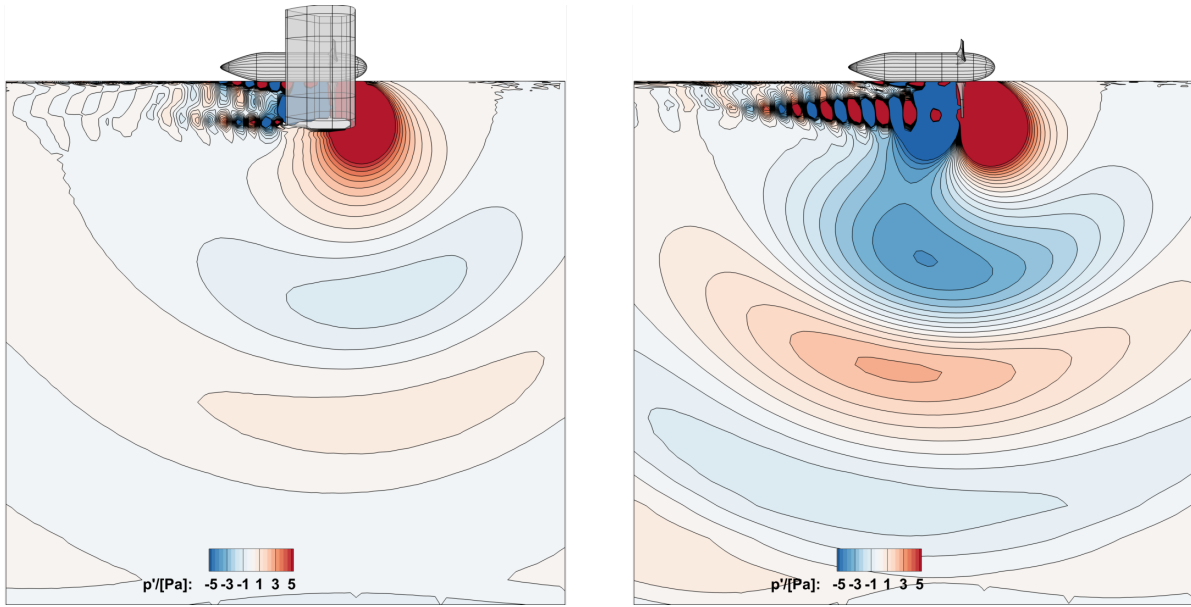
This section describes the near- and far-field acoustics of the ducted/un-ducted propellers at the advance ratio of  $\mu = 0.191$  based on the high-fidelity results, while the two configurations produce the similar amount of aerodynamic loads. The near-field acoustics was calculated by directly extracting the acoustic pressure field from the CFD results, hence both surface and volume acoustic sources including broadband components were considered. The far-field acoustics was calculated using the Farassat Formulation 1A as detailed in Section II, and took the CFD results of surface pressure fields as input. This approach considers only surface terms by the thickness and loading components, but is suitable for the current study in the far-field in the sub-sonic region and has been widely adopted in previous studies of open and ducted rotor acoustics [36–38].

### *Near-field Acoustics*

The near-field acoustics is of interest as it strongly affects cabin noise. It also determines the source of far-field noise propagation. In the present work, the near-field acoustics in close proximity to the ducted and un-ducted propellers was directly extracted from high-fidelity CFD simulations. Pressure signals at microphone points were recorded, and the mean values were subtracted to obtain the acoustic pressures. Overall Sound Pressure Levels (OSPL) were then derived and analysed.

A first analysis was made on the *Azimuth* =  $0^\circ$  slice at  $\mu = 0.191$ . The sound pressure fields of the ducted/un-ducted were extracted directly and the instantaneous sound pressure contours on the *azimuth* =  $0^\circ$  planes are shown in Figures 5(a) and 5(b). The acoustics generation and propagation are shown clearly, including components by the tip vortices and aerodynamic interactions. It can be seen that the ducted propeller tip vortices contribute a minor part to the overall acoustics and lasts for only about 3 blade radii, while the open propeller tip vortices cause high pressure fluctuations and extends to about 6 blade radii downstream. The open propeller sees generally higher pressure fluctuations. Patterns of the acoustic propagation to the far-field are also different due to the duct presence. It can be seen in Figure 5(a) that the duct blocks the propeller acoustics and allows the emission mostly from the inlet lip.

To further study the near-field acoustic directivity features around the ducted/un-ducted propellers, we extracted signals on spheric receiver array and cylindrical receiver arrays enclosing the propulsor. Here we show only acoustic results from the cylindrical array, since acoustic features on both arrays are very similar. The receiver surface is twice the blade radius away from the centre of rotation surrounding the propulsor as shown in Figure 6(a), a scenario where typically the cabin noise is perceived. The corresponding OSPL results are shown in Figures 6(b) and Figure 6(c). For the ducted propeller, the peak OSPL stands at about 105 dB in a small region near the duct inlet. For the open propeller,

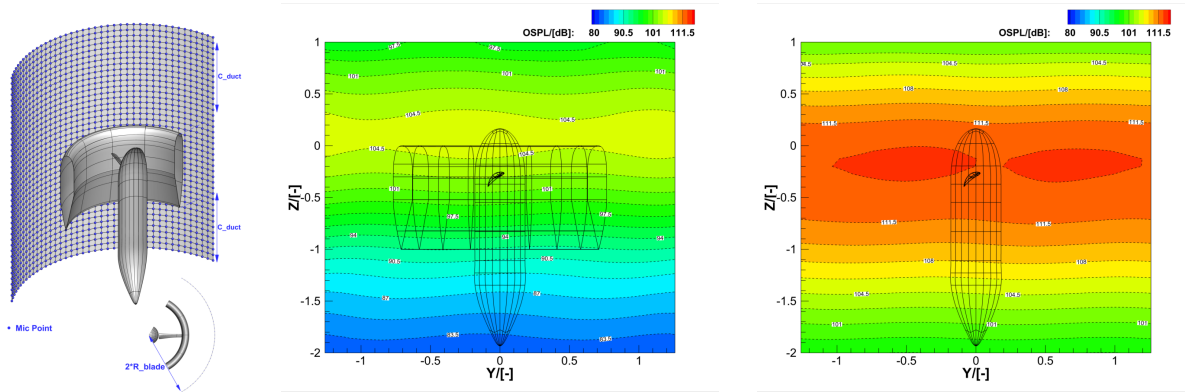


(a) Instantaneous sound pressure contours of the ducted propeller on the *Azimuth* = 0° plane at  $\mu = 0.191$ .

(b) Instantaneous sound pressure contours of the un-ducted propeller on the *Azimuth* = 0° plane at  $\mu = 0.191$ .

**Fig. 5** Instantaneous sound pressure contours at the *azimuth* = 0° slice for the ducted/un-ducted propellers at  $\mu = 0.191$ .

the peak value stands at about 115 dB in a larger region near the propeller disk. These show again the duct acoustic shielding effects in the near-field.



(a) Cylindrical microphone array around the propulsor.

(b) Near-field OSPL contours of the ducted propeller on the surface in Figure 6(a) at  $\mu = 0.191$ .

(c) Near-field OSPL contours of the un-ducted propeller on the surface in Figure 6(a) at  $\mu = 0.191$ .

**Fig. 6** Near-field OSPL contours on the cylindrical receiver surface at  $\mu = 0.191$  for the ducted and un-ducted propellers.

Overall, the ducted propeller produces lower OSPL levels than the un-ducted configuration by about 10 dB in the near-field for the case studied. The near-field acoustic directivity features are also altered. Due to the blockage effect of the duct, the acoustic peaks are redirected to directions of the duct inlet and outlet.

### *Far-field Acoustics*

The far-field acoustics of the ducted/un-ducted propellers was analysed using an in-house acoustic code based on the classic FW-H equation solved with Farassat Formulation 1A, as detailed in Section II. The CFD solutions of the surface pressure fields were used as the input for the acoustic tool. The centre-body was not included in the far-field acoustic calculation, as its contribution is regarded as minor due to the low loading.

As stated in Section II, the current implementation of the far-field acoustic prediction is an extension of the existing acoustic code HFWH[37] in the high-level language Julia. Extensive code-to-code comparisons have been performed in order to verify the current implementation. Regardless, to further validate the current acoustic tool, a ducted propeller acoustic test case by Hubbard [10] was adapted. The experiments measured the acoustics of different propeller/duct combinations in hover. Although the model size was large (4-foot-diameter blades), the acoustic tests were performed outdoors and the results were affected. The acoustic directivity was measured 30 ft away from the centre of rotation, all around the propulsor, on the ground. The tests provided no loading measurements other than the duct thrust through sectional pressure integrations, hence the case is not ideal for aerodynamic or acoustic validation as large uncertainties must be expected. Regardless, this case is the most suitable among the very few experimental studies concerning acoustics of large ducted fans.

Comparisons between numerical and experimental results of the ducted propeller acoustic directivity for the Hubbard case [10] are presented in Figure 7. Note that the experiments measured the acoustics at ground level, while ground effects were not considered neither in the CFD simulation or the acoustic calculation. Despite all uncertainties, the agreement between the numerical prediction and the test data is still favourable, with OSPL values of about 90 to 95 dB at this distance. This strengthens our confidence of the present acoustic tool and strategy for the noise prediction of ducted propellers.

Acoustic calculations of the ducted/un-ducted propellers of Grunwald [8] were later conducted at 400 evenly-distributed microphones on a full sphere enclosing the propulsor, 20 duct chords away from the centre of rotation, to investigate the far-field acoustic directivity. The results are shown in Figure 8. For both configurations, the acoustics varies little along the propeller azimuth, hence detailed comparisons of the directivity features are made on the azimuth station of  $0^\circ$ . Also, for both configurations the loading components contribute the most to the total noise.

As shown in Figure 8, the un-ducted propeller produces almost evenly distributed acoustics along all directions around at about 80 dB, with a small increase to about 85 dB between  $-40^\circ$  to  $30^\circ$  directivity angles. This is consistent with its near-field acoustic features that the peak noise is around and slightly after the propeller disk ( $0^\circ$  directivity angle). As for the ducted propeller, its noise around  $-90^\circ$  and  $90^\circ$  is almost the same as for the un-ducted at about 80 dB. However, in the range between  $-70^\circ$  and  $60^\circ$ , the acoustic level is clearly lower than the un-ducted counterpart by up to 15 dB. The lowest acoustic level is perceived at  $-30^\circ$  at about 65 dB, while a local maximum is noted at around  $15^\circ$  at about 75 dB. These features are also consistent with the near-field acoustic patterns of the ducted propeller that the

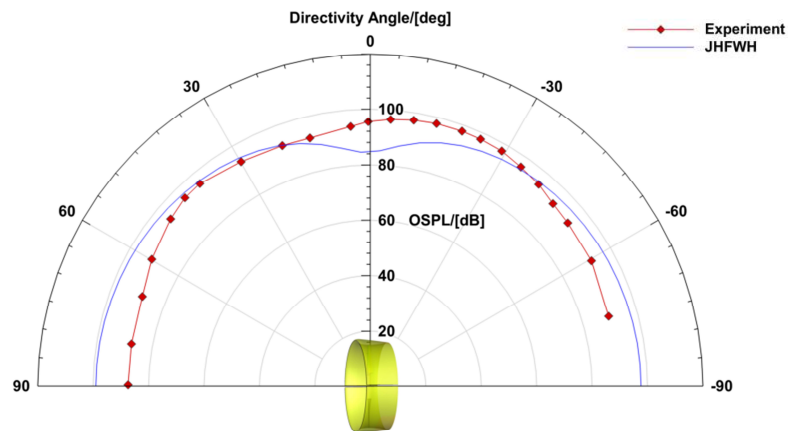


**Fig. 7 Comparisons between numerical and experimental results of the ducted propeller acoustic directivity 30 ft away for the ducted propeller of Hubbard [10].**

acoustics is blocked by the duct.

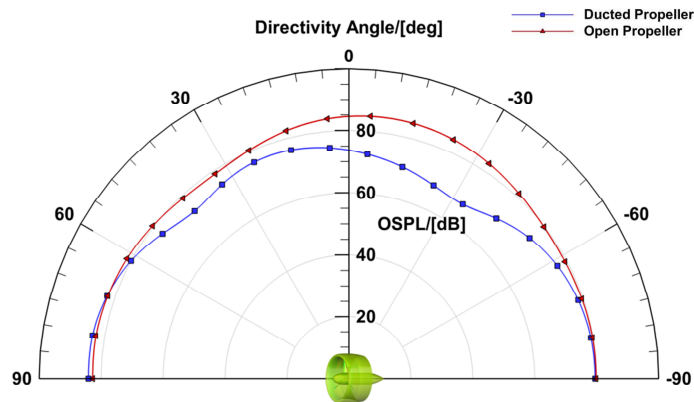
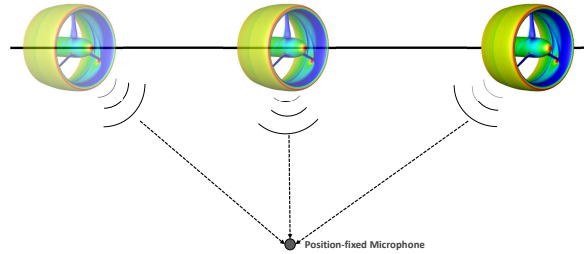


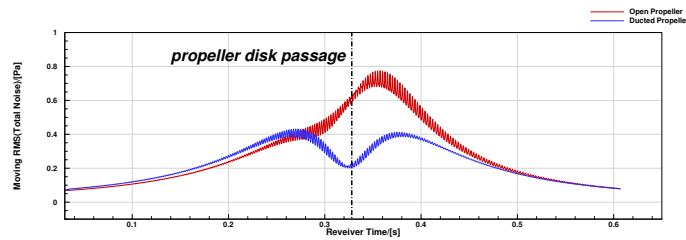
**Fig. 8 Total noise OSPL directivity of the ducted/un-ducted propellers noise signals at 20 duct chord away ( 90° is the inflow direction).**

The fly-by noise, i.e. the noise signals recorded by ground-fixed microphones while the propulsor or aircraft is flying over, was also calculated. The scenario is illustrated in Figure 9(a) with the microphone fixed while the ducted propulsor flies over. This scenario is often encountered in certification tests. The noise calculations employed the same FW-H equation and Farassat 1A formulation, with changes of relative positions between acoustic panels and receiver points accounted for. The acoustic signals for the Grunwald ducted/un-ducted propellers were calculated while flying over fixed microphone 10 and 20 duct chords below. The propulsors started from [0, 0, 0] (in m) and was translating in Z direction with a constant speed of 30.48m/s. The microphones were fixed at [2.619, 0, 10] (in m) and [5.238, 0, 10]

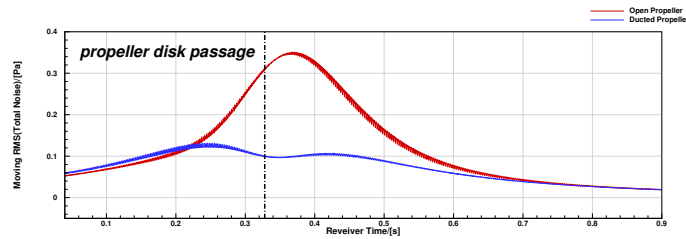
(in m), corresponding to 10 and 20 duct chords below the propulsors. The propeller disk was right above the receiver points about 0.328s after starting.



(a) Illustration of the microphone position and the propulsor motions for the fly-by noise calculation. The microphone was fixed while the propulsors were translating in the arrow direction.



(b) Moving RMS values of the acoustic signals recorded at the receiver point 10 duct chords below for the ducted/un-ducted propellers.



(c) Moving RMS values of the acoustic signals recorded at the receiver point 20 duct chords below for the ducted/un-ducted propellers.

**Fig. 9 Fly-by noise calculations at fixed receiver points. The vertical line denotes the time point when the propeller disk was right above the receiver point.**

The moving root-mean-square (RMS) values of the acoustic signals were calculated and are presented in Figures 9(b) and 9(c). The moving RMS values were calculated using signals within a time window of one propeller revolution, i.e. 0.0075s, at each time point. For the un-ducted configuration in Figure 9(b), the averaged peak is slightly after the propeller passage. This agrees with the previous near- and far-field acoustic directivity analysis for the un-ducted propeller that noise peaks are seen at and slightly after the propeller disk. For the ducted propeller, however, 2 acoustic peaks can be noticed ahead and after the blade passage. The first peak is only slightly higher than the second. A valley in the signal is noted near the passage. At 20 duct chords away as shown in Figure 9(c), the features are very similar but

show lower strength and fluctuations. The ducted features remain very similar at this position with the low noise region noted during the blade passage. These agree well with the previous near- and far-field acoustic directivity investigations for the ducted propeller. The duct blocks the acoustic propagation directly from the propeller disk and redirects the acoustics to the duct inlet and outlet directions. In general, the peak acoustic strength of the ducted configuration is only a quarter or half the magnitude of the un-ducted. In addition, a low noise slot is generated during the propeller passage by the ducted propeller. This feature can be further used in flight path optimisation to minimise the acoustic perception at specific locations such as communities.

#### IV. Adjoint-based Ducted Propeller Optimisation

As presented in the previous section, at  $\mu = 0.191$  (with  $RPM = 8000$  and  $\beta_{0.75} = 29.58^\circ$ ), the ducted/un-ducted configurations of Grunwald [8] show similar aerodynamic performance at this operating condition, with the ducted propeller producing slightly higher thrust at lower torque. This advance ratio typically corresponds to the speed of a tilt-duct VTOL aircraft about to leave transition and enter level flight[8]. Higher propulsor performance capacity is important for safer transition. Our previous performance investigations [2] show that this test condition is very close to the critical advance ratio, with the same rotating rate and pitch setting, beyond which the ducted propeller becomes less efficient than its un-ducted counterpart due to the increasing duct drag. Optimisation at this operating point is hence necessary for improved ducted propeller performance capacity. an adjoint-based optimisation framework is adopted to improve the ducted propeller performance at this  $\mu = 0.191$  by altering the duct and blade shapes, as has been detailed in Section II. The acoustics is not involved directly in the optimisation objectives/constraints, as the aerodynamic performance is the primary concern. Nonetheless, the acoustics of the optimised designs was found to be good.

The objective was set to increase the thrust subject to torque constraints. The overall efficiency of the propulsor was not constrained, since we were more interested in expanding the performance capacity at this operating condition for the transition. Besides, such objective and constraint settings were expected to deliver larger changes in the geometry and flow-field, which is beneficial for the study of how duct/blade shape changes affect the overall performance. This will provide more guidance on ducted propeller designs and pave the way for future investigations of variable-geometry duct for propulsor performance control, which combines with classic pitch control approach will extend greatly the performance space of ducted propellers. The current optimised designs were hence examined at different pitch settings compared with the pitch variation study of the initial ducted/un-ducted propellers. The optimisation results were also examined at different advance ratios and cross-wind angles.

The test matrix of the optimisation study is presented in Table 4. The optimisation was first performed on the duct inlet/outlet shapes with the blade twist fixed, and on the blade twist with the duct shape fixed. Note that the blade twist deformation in this study included pitch variations. Hence the blade twist optimisation in this study offers optimal twist distribution, and new global pitch settings for the set objective. Optimisation was afterwards carried out with the duct

outlet shape and the blade twist allowed to change at the same time. This was due to the consideration that the duct and propeller form a coupled system with significant aerodynamic interferences. The coupled optimisation is expected to provide larger performance improvement.

The optimisation calculations were performed on coarse grids of about 4 million cells for lower computational costs. The optimisation results were later verified using finer grids to reduce uncertainties, and minor differences were noted. Each optimisation case converged after about 10 to 15 iterations. Each optimisation iteration involved a CFD calculation of the flowfield, and occasionally the sensitivity calculation through adjoint methods. The adjoint calculation is of the similar cost to the flow calculation, but whether the calculation was conducted at each iteration was decided by the optimiser. The initial baseline flow calculation took about 6 hours using 32 cores, while successive CFD calculations in each iteration took only 1 hour, restarting from previous solutions. Considering the amount of design variables involved and comparing to meta-model-based optimisation, the current adjoint-based optimisation implementation has saved the time and resources for extra hundreds of CFD cases.

**Table 4 Test matrix for the adjoint-based ducted propeller optimisation.**

Case	Design Variables	Configuration	Objective	Constraints	Advance Ratio	RPM	Blade Pitch ( $\beta_{0.75}$ )[deg]
1	Duct Inlet/Outlet	Ducted Propeller		110% torque			29.58
2	Blade Twist(Pitch)	Ducted Propeller	Maximised Thrust	120% torque	0.191	8000	-
3	Duct Outlet & Blade Twist (Pitch)	Ducted Propeller		120% torque			-

### A. Optimisation Results and Shape Deformation

Results of the optimisation cases of Table 4 are summarised in this section. The duct deformation through the duct shape optimisation and the coupled duct/blade optimisation, i.e. case 1 and 3 in Table 4, are presented in Figure 10 along with the original design. The leading-edge and trailing-edges were allowed to offset within a circle of  $0.1C$  radius. The duct shape was allowed to deform except for the region between  $x/C = 0.2$  to  $0.53$ . Note the duct inlet shape was not involved in the coupled optimisation case (case 3). The blade pitch distributions of the blade twist optimisation (case 2) and the coupled optimisation (case 3) are shown in Figure 11 along with the original distribution. The performance changes with respect to the original design are shown in Table 5.

For the optimisation of the duct inlet and outlet shapes, 16 design variables were used in the current study, 4 for the leading-/trailing-edge point offsets and 12 for the leading-/trailing-edge shapes. The convergence history of the duct inlet/outlet shape optimisation is presented in Figure 12. As can be noted, the optimisation converged in about 14 loops subject to the inequality constraint, indicating the efficiency of the adjoint-based CFD optimisation. As in Table 5, by altering the duct shape, the thrust was increased by about 8.2% subject to the constraint of 110% torque. The propulsor efficiency was reduced very slightly by about 1.6% for this thrust increase.

The optimisation brought both leading- and trailing-edges inwards, as shown in Figure 10, decreasing the expansion

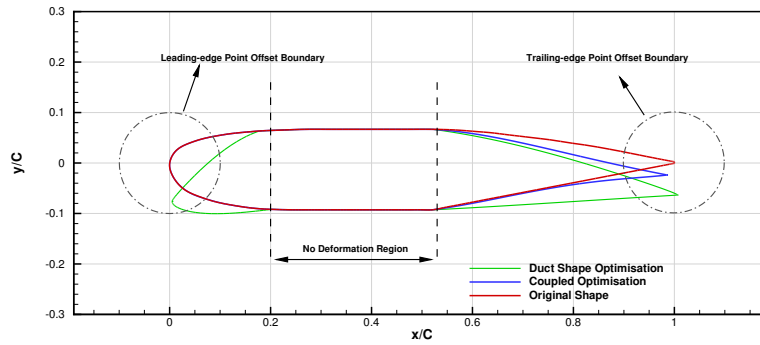


**Fig. 10** Illustration of the duct shape deformation through the duct shape optimisation and coupled duct exit and blade twist optimisation. Note only the duct exit was involved in the coupled optimisation.

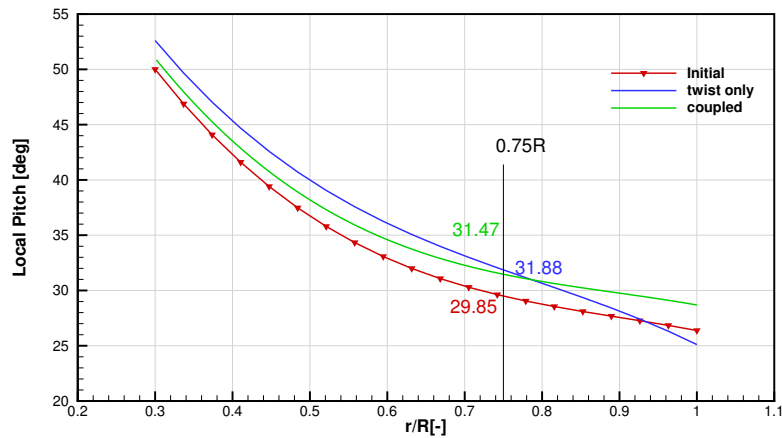


**Fig. 11** Illustration of the blade pitch distribution changes through the blade twist optimisation and coupled duct exit and blade twist optimisation.

**Table 5** Performance changes through optimising different components. The changes are denoted by variations with respect to the original corresponding values.

Case	Optimisation Component	Thrust Changes	Torque Changes	Efficiency Changes
1	Duct Shape	8.2%	10.0%	-1.6%
2	Blade Twist	11.6%	20.0%	-7.0%
3	Coupled Duct Shape & Blade Twist	18.3%	20.0%	-1.4%

ratios of the duct inlet and outlet. The duct camber was hence reversed compared to the original design. Only very small offsets are noticed for the leading-/trailing-edge points, hence the chord length remains the same. The inner surface of the duct is now almost flat and conforming with the mid-chord part, with a slightly expanded diffuser exit. In general,

the optimised shape is expected to induce lower flow rates through the propeller disk and improves the inflow conditions for the propeller, increasing the propeller and the total thrust.

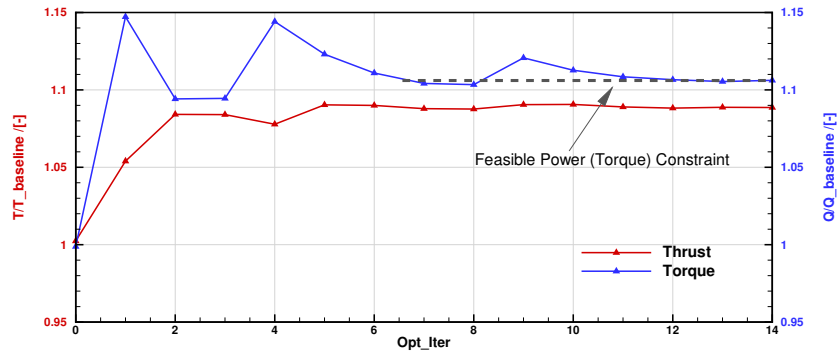


**Fig. 12 Optimisation convergence history of the duct inlet/outlet shapes with torque constraint.**

The current optimisation of the blade twist (case 2) involved 4 design variables, i.e. the Bernstein coefficients describing the pitch distribution along the blade span. The coupled optimisation (case 3) of the duct exit and blade twist involved 12 design variables, 4 for the twist, 2 for the trailing-edge point offsets, and 6 for the trailing-edge shapes. Note that only the duct diffuser was involved in this study, in order to reduce the number of design variables. The objective was again set to increase the thrust subject to a 120% torque constraint.

The convergence history of both optimisation studies is presented in Figure 13. The blade twist optimisation converged in 6 loops as fewer design variables were involved. As in Table 5. With the 120% torque constraint, only optimising the blade twist delivered a thrust increase of about 11.6%. For such a thrust increase, the efficiency was penalised by about 7%. The corresponding optimised pitch distribution is shown in Figure 11. Comparing to the original design, the optimised blade has constantly increased blade pitch by about  $2^\circ$  throughout the span except for the tip. Beyond the 75% span, the blade is highly twisted resulting in lower pitch at the tip. The global pitch increase is expected in order to accommodate the high axial velocity at this advance ratio. The twist changes are similar to optimisation results of conventional open rotor twist, where typically the twist is increased to offload the tip region for higher efficiencies. However, in the current ducted propeller case, only minor changes in the efficiency are observed.

As in Figure 13, the coupled optimisation took about 10 iterations to converge with 12 design variables. Subject to the same torque constraint, however, the coupled optimisation managed to increase the thrust by about 18.3%, and for this large thrust increase the efficiency was very slightly decreased by about 1.38%. The duct deformation is presented in Figure 10. Note the inlet shape was not included to reduce the amount of design variables and to reduce the computational cost. The duct diffuser is allowed to deform for  $x/C > 0.53$  (see Figure 10). The trailing-edge point is moved slightly reducing the expansion ratio, and very slightly the chord length. The lower expansion ratio at this high advance ratio of 0.191 is reasonable as it reduces the duct-induced axial flow rates through the propeller disk

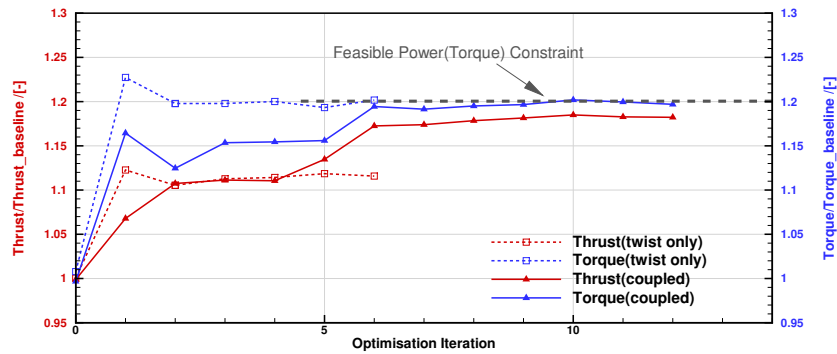


**Fig. 13 Optimisation convergence history of the coupled duct outlet shape and the blade twist with torque constraint.**

and improves the propeller inflow condition. The optimised blade pitch distribution is shown in Figure 11. The pitch angles are slightly increased by about  $1^\circ$  from the root to about the 60% span. Larger pitch angle increases by about  $2^\circ$  to  $3^\circ$  towards the tip. Therefore, the blade twist is indeed eased, in contrast to conventional open rotor optimisation. Nevertheless, combining with the duct shape change, such blade changes bring higher performance improvement. It is also noted that the changes in the pitch distribution and the duct shape are generally small, yet the thrust increment is large. It can be hence argued that the coupled deformation of the duct shape and blade twist bring a larger performance capacity for the ducted propeller to accommodate variable operating conditions and requirements.

## B. Performance and Flow-field Acoustic Analysis of the Optimised Designs

In practice, the thrust increase is mostly realised by conventional pitch increases. Therefore, the optimisation results are compared with the thrust-torque map of the original design at  $\mu = 0.191$  subject to pitch variations as shown in Figure 14. Blade pitch variations were also applied to the coupled optimisation case to examine the performance of the new designs at different disk loadings. Compared to the original design, for the same thrust required, the duct shape optimisation (Case 1) produces almost the same torque, while the blade twist optimisation (Case 2) generates slightly lower torque. The coupled duct/blade optimisation (Case 3) shows the greatest improvement with a large torque reduction. Performance variations of the coupled case were also examined at different disk loadings by blade pitch variations as shown in Figure 14. The coupled optimisation brings much better performance at higher pitch settings/disk loadings with lower torque, while the performance at lower disk loadings is similar to and slightly lower than the original design.

Performance of the coupled optimisation (Case 3) was also examined at other advance ratios of  $\mu = 0.0955$  and  $\mu = 0.382$  and compared with the original open propeller and ducted propeller, as shown in Figure 15. The advance ratio was changed by varying the free-stream speed while keeping the rotating rate constant. The initial coupled optimisation (Case 3) managed to produce higher thrust at higher and lower advance ratios than the original ducted propeller, although

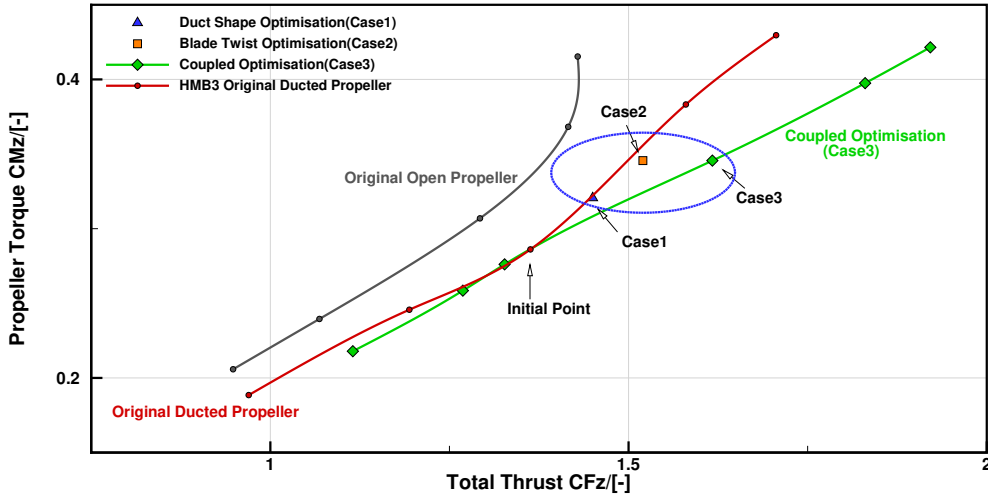


**Fig. 14 Thrust-torque map of the original ducted/un-ducted Grunwald[8] propellers at  $\mu = 0.191$  subject to blade pitch variations. Performances of the optimised cases are also plotted using scatters.**

at higher torque costs. The blade pitch of the coupled optimisation case was later reduced by  $-2.5^\circ$  to deliver similar thrust level as the original design at  $\mu = 0.191$ . At this reduced blade pitch required slightly larger power input for the similar thrust comparing to the original design. The optimised design also showed slightly penalised performance than the original at the lower advance ratio of  $\mu = 0.0955$ . This was expected as the reduced duct expansion ratio is more beneficial at higher advance ratios. Its thrust at the very high advance ratio of  $\mu = 0.382$ , although still close to zero, was improved than the original design, which is producing negative thrust. At this high advance ratio, the duct causes large drag rather than propulsion due to the fast free-stream and low propeller induction, so increasing the blade pitch at high advance ratios is still necessary[2].

In order to examine the crosswind performance of the optimised designs, initial simulations of the duct optimisation (Case 1), where large duct shape deformation was observed, with non-axial inflows were also performed. Performance comparisons, in terms of lifting forces  $C_l$  and propulsion forces  $C_{F_z}$ , are presented in Figure 16. It can be seen that at  $AoA = 20^\circ$ , the optimised duct shape produces the similar amount of lift and slightly lower propulsion. This suggests that the crosswind performance of the optimised design is only very slightly penalised, despite the large shape changes which improve its axial performance.

The component and total thrust changes of the optimised designs are shown in Table 6. The thrust changes are denoted by the relative variations with respect to the original corresponding thrust, i.e.  $\delta T = \frac{T_{opt}}{T_0} - 100\%$ , where  $T_{opt}$  is the new component or total thrust through optimisation, and  $T_0$  is the original component or total thrust. The component contributions are represented as the ratio of the component thrust to the total thrust, i.e.  $\frac{T_{com}}{T_{total}} \times 100\%$ , where  $T_{com}$  is the component thrust and  $T_{total}$  is the total thrust.

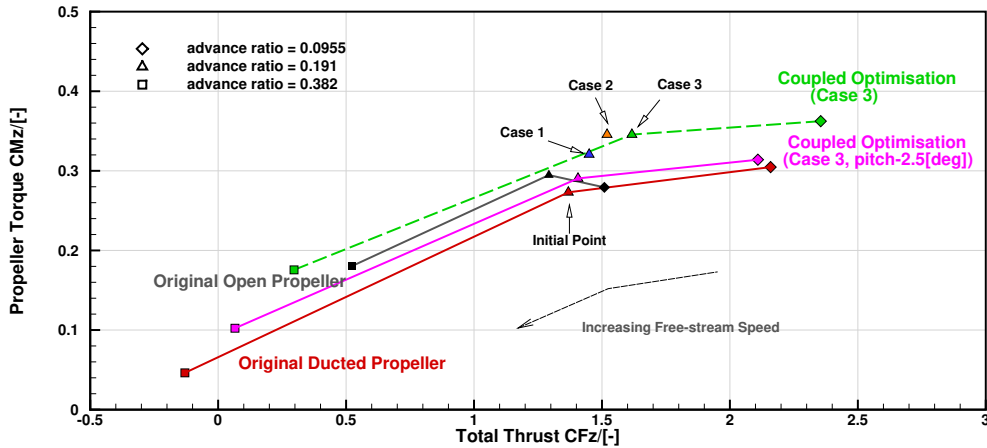


Fig. 15 Performance comparisons between the optimised designs and the original designs at different advance ratios at initial pitch settings.

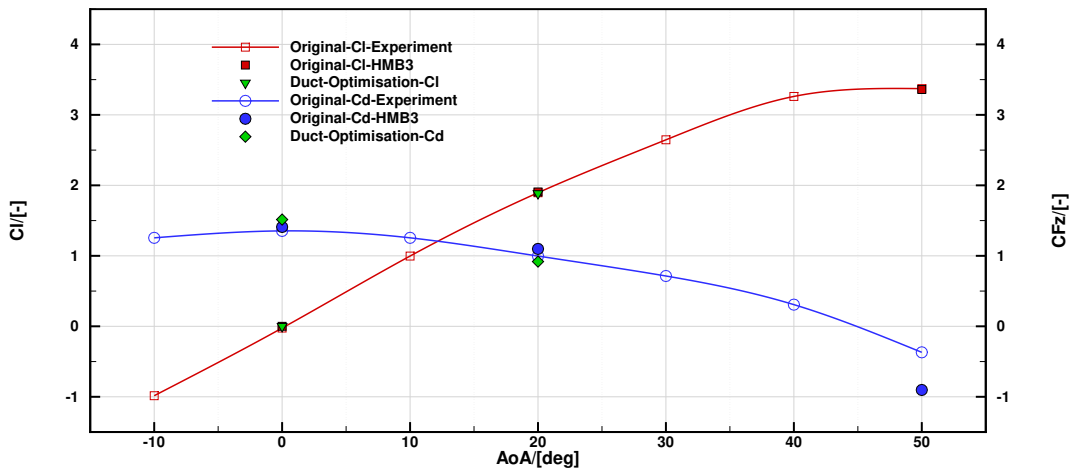


Fig. 16 Performance comparisons between the optimised duct design (case 1) and the original design at crosswind.

As seen in Table 6, different optimisation strategies brought various thrust distributions upon components of the ducted propeller. For the duct shape optimisation, the propeller thrust was increased by 27.1% while the duct and centre-body thrust was decreased by about 40.7%, and the total thrust was increased by 8.2% subject to the 110% torque constraint. The propeller disk was hence heavily loaded with 84.7% of the total thrust carried. For the blade twist optimisation, the propeller thrust was increased by 9.2% while the duct thrust was also increased by 17.8%, and the total thrust was increased by about 11.6% subject to the 120%. The increases in both propeller and duct thrust have also been noticed in a previous pitch variation study [2] due to the increased propeller suction. The thrust ratio between the propeller and the duct was changed only very slightly comparing to the original design. For the coupled optimisation of the duct trailing-edge and blade twist, the propeller thrust was increased by about 20.6% while the duct thrust was

increased by 12.5%, and the total thrust was increased by about 18.3% subject to the 120% torque constraint. The propeller loading was increased slightly carrying about 73.5% of the total thrust.

**Table 6 Thrust changes of the ducted propeller components through optimisation of the duct shape and blade twist. The thrust changes are denoted as  $\delta T = \frac{T_{opt}}{T_0} - 100\%$ , where  $T_{opt}$  is the new component or total thrust through optimisation, and  $T_0$  is the original component or total thrust. The thrust contributions are represented as  $\frac{T_{com}}{T_{total}} \times 100\%$ , where  $T_{com}$  is the component thrust and  $T_{total}$  is the total thrust.**

Case	Optimisation Component	Propeller Thrust Change/[N]	$\delta T$ /[%]	Contribution/[%]	Duct&Centre-body Thrust Change/[N]	$\delta T$ /[%]	Contribution/[%]	Total Thrust Change/[N]	$\delta T$ /[%]
1	Duct Shape	16.60	27.1%	84.7%	-10.41	-40.7%	15.3%	7.12	8.2%
2	Blade Twist	5.65	9.2%	70.6%	4.56	17.8%	29.4%	10.09	11.6%
3	Duct Shape & Blade Twist	12.62	20.6%	73.5%	3.21	12.5%	26.5%	15.94	18.3%

The instantaneous flow-fields are presented in Figures 17(a) to 17(h) using contours of pressure coefficients and normalised axial velocities at the *azimuth* = 0° slice. The pressure coefficients were calculated using the free-stream velocity and the ambient pressure. The axial velocity is normalised by the free-stream axial speed. Note the axial flow travels towards the -Z axis. The flow-field of the original design is presented in Figures 17(a) and 17(b) for comparisons.

Flow-fields of the duct optimisation are shown in Figures 17(c) and 17(d). As can be noted in Figure 17(c), the propeller disk saw a larger high pressure area towards the blade root. The propeller disk hence carried higher loadings. Further, as shown in Figure 17(d), the axial velocity through the propeller disk was slowed comparing to the original design in Figure 17(b). Given the same blade shape and the constant RPM during the duct shape optimisation, it can be concluded that the propeller thrust was increased due to the improved inflow condition because of the duct deformation. The deformed duct shape is expected to induce lower mass and momentum flow rates through the propeller disk, which is necessary at high advance ratios and has been noted in Figure 17(b).

Flow-fields of the blade twist optimisation are shown in Figures 17(e) and 17(f). In Figure 17(e), it can be seen that the blade also saw a larger high pressure region towards the root area and the propeller disk loading was hence increased. From Figure 17(e), the axial velocity through the propeller disk was slightly increased compared to the original design in Figure 17(b), except that faster flow was seen through the mid-span and root regions in the optimised case. In other words, the axial velocity was more evenly distributed along the blade radius comparing to the original case. These are consistent with the blade pitch and twist changes from the optimisation as shown in Figure 11. Since the global pitch was increased by about 2°, which is reasonable for propeller at high advance ratios and higher thrust was hence expected. Further, with the increased blade twist at the tip, higher loadings were hence expected at mid-span and root regions, and the wake was expected to be more evenly distributed approaching the uniform wake distribution for an ideal rotor. The duct thrust was also increased due to the higher propeller suction.

Flow-fields of the coupled duct exit and blade twist optimisation are presented in Figures 17(g) and 17(h). It can be

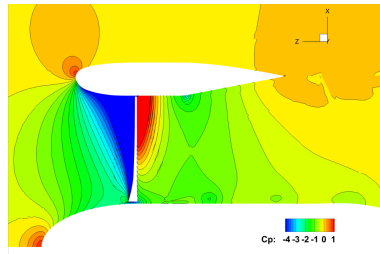
noted from Figure 17(g) that the blade saw a higher loading through the optimisation. The axial velocity, as in Figure 17(h) was slightly increased comparing to the original design in Figure 17(b). Comparing to the original design, the blade pitch was increased along the span, especially at the tip. This is reasonable due to the high advance ratio and the high inflow velocity. Comparing to the separate blade twist optimisation, the local pitch angles in the coupled optimisation were lower at the root and mid-span regions, but the angles were higher beyond  $0.8 r/R$ . This is not favourable for the propeller efficiency from simple theoretical analyses. Nevertheless, the coupled optimisation managed to offer about 7% more thrust than the separate blade twist optimisation. This should be owing to the slightly reduced duct exit expansion ratio that improves the inflow conditions for the propeller disk. Also, small coupled deformation of the blade and duct leads to large performance changes. This indicates a larger performance capacity of the ducted propeller to cover various operating conditions and requirements using the coupled deformation.

Overall, it can be concluded that the duct shape optimisation and blade twist optimisation increase the total propulsor thrust at this high advance ratio of  $\mu = 0.191$  in different ways. At this high axial speed, the duct deformation reduces the induced flow rates through the propeller disk, hence creates a more favourable working condition for the propeller at high speeds. The duct-propeller thrust distribution is also altered. **In a different perspective, it is possible to use the duct deformation for the performance control of ducted propellers, by altering the propeller inflow conditions and the thrust distribution between the duct and the propeller. However, issues regarding mechanism complexity, control response, structure etc. must be accounted for, beforehand.** The blade twist optimisation adjusts the local pitch angles for the blade elements to accommodate high inflow velocities and improve the efficiency by redistributing the loads among the propeller disk. The coupled deformation of the duct shape and blade twist combines both means and offers larger and more sensitive overall performance changes.

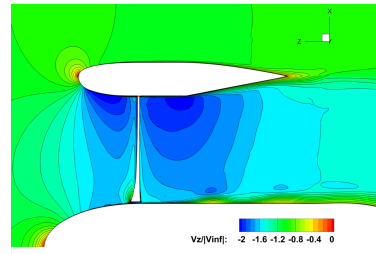
### C. Far-field Acoustics of Optimised Shapes

The far-field acoustic performances of the optimised designs were also examined to explore changes brought by the duct shape and blade deformation. The far-field acoustics was calculated at microphone points on a spherical surface of 20-duct-chord radius surrounding the propulsor to investigate the directivity, the same as in Section III.

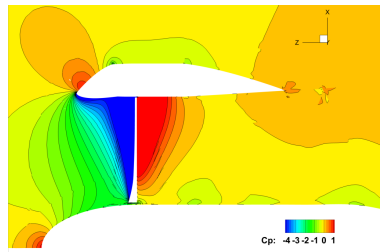
**The OSPL values of the total noise signals for the original and optimised designs are presented in Figure 18. The acoustic levels vary little along the propeller azimuth, hence comparisons are made at the azimuth station of  $0^\circ$ . Comparing to the original open propeller, the optimised designs still show similar acoustic levels along the axial directions and lower levels in a large range between  $-60^\circ$  to  $60^\circ$ . Comparing to the original ducted propeller, the acoustic levels are maintained similar but variations in directivities are noted due to design changes, especially in the duct shape. For the blade twist optimisation (Case 2), the acoustic directivity is almost identical to that of the original design. The duct shape optimisation (Case 1) and the coupled optimisation (Case 3) mostly shifted the location of the local acoustic minimum towards the inflow direction while maintaining the minimum values still at around 65 dB. The**



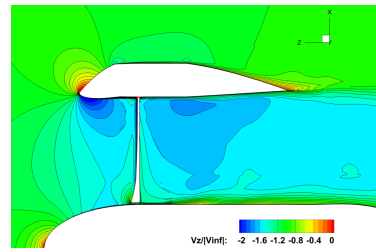
(a) Pressure coefficient contours of the original design. The pressure coefficients are normalised using the free-stream velocity.



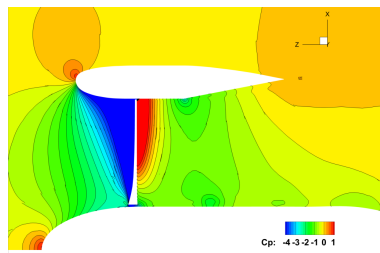
(b) Axial velocity contours of the original design. The values are normalised by the free-stream axial velocity.



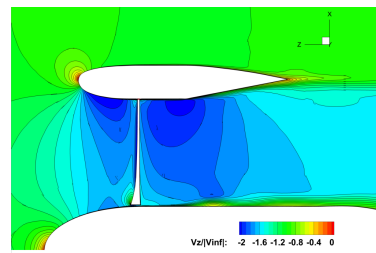
(c) Pressure coefficient contours of the duct shape optimised design. The pressure coefficients are normalised using the free-stream velocity.



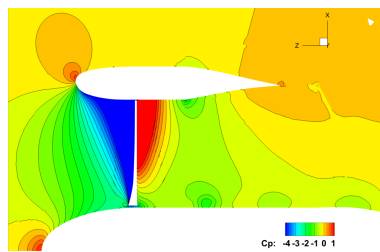
(d) Axial velocity contours of the duct shape optimised design. The values are normalised by the free-stream axial velocity.



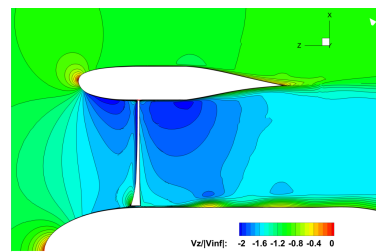
(e) Pressure coefficient contours of the blade twist optimised design. The pressure coefficients are normalised using the free-stream velocity.



(f) Axial velocity contours of the blade twist optimised design. The values are normalised by the free-stream axial velocity.



(g) Pressure coefficient contours of the coupled duct shape/blade twist optimised design. The pressure coefficients are normalised using the free-stream velocity.



(h) Axial velocity contours of the coupled duct shape/blade twist optimised design. The values are normalised by the free-stream axial velocity.

**Fig. 17** Flow-fields of the original and optimised shapes on  $y = 0$  slice.

duct shape optimisation moved the lowest acoustic level to around  $0^\circ$  directivity, while the coupled optimisation moved the lowest to around  $15^\circ$  directivity. Overall, it can be seen that the duct shape plays a more significant role, comparing to the blade design, in the far-field acoustic pattern of the ducted propeller.

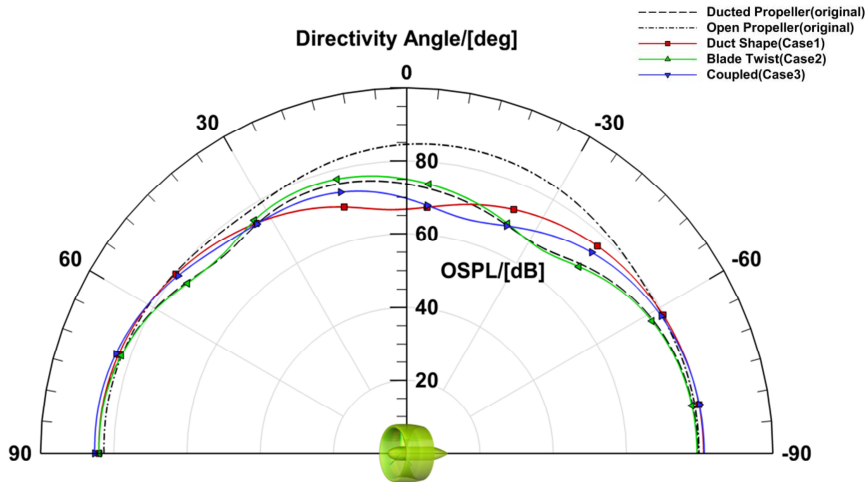


**Fig. 18 Far-field acoustic directivity spheres (20 duct chords away) of the optimised designs.**

The perceived noise signals at fixed ground positions were also calculated for the optimised designs and compared with the original ducted/un-ducted designs. The microphone position was placed at 10 duct chords below as illustrated in Figure 9(a). The moving RMS values of the acoustic signals were calculated using signals within a time window of one propeller revolution and are presented in Figure 19. Acoustic magnitudes of all three optimised designs are very similar to that of the original ducted propeller and are only a quarter or half the strength of the un-ducted. The moving RMS of the optimised designs are also mildly smoother than the original design. Two acoustic peaks are still noticed, respectively before and after the propeller passage. The acoustic valley is also noted at the propeller passage. For the duct shape optimisation, the moving RMS of the signal has similar peak values to the original, but has a lower minimum. The signal is also slightly phase-shifted with the second peak delayed. The moving RMS of the twist optimisation is almost identical to the original. For the coupled optimisation, the moving RMS peaks are slightly higher than the that of the original, the valley value is also lower regardless. These suggest that the duct shape plays a significant role in the ducted propeller acoustics. It is hence also possible to alter the acoustic performance by changing the duct shape. In combination with blade twist deformation or pitch regulation, the aerodynamic performance may not be penalised for this purpose.

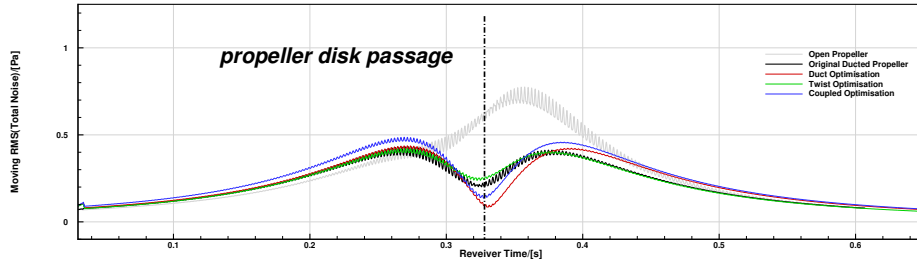


**Fig. 19** Moving root-mean-square (RMS) values (calculated using signals within a time window of one blade rotation, i.e. 0.0075s, at each time point) of the fly-by acoustic signals recorded 10 duct chords below (Figure 9(a)) of the optimised designs.

## V. Conclusions

This work presented numerical investigations of the acoustics and performance optimisation of ducted/un-ducted propellers. The aerodynamic performance of the Grunwald ducted propeller test case is well predicted by the HMB3 CFD simulations. Favourable agreement between numerical results and experimental data, despite uncertainties in geometries, measurements, and conditions, is achieved. Near-field flowfields of the ducted/un-ducted propellers are resolved in detail by the high-fidelity methods, and near-field acoustic fields are extracted directly from the CFD results. Reasonable agreement with experimental data for the far-field acoustic predictions is also obtained. The far-field acoustics of the ducted/un-ducted configurations calculated through the FW-H equations upon the CFD solutions show fine consistency and correlation with the near-field acoustic features. The effectiveness and the efficiency of the proposed adjoint-based optimisation framework has been demonstrated. It improved the Grunwald ducted propeller performance by altering the duct and blade shapes generally within 10 to 15 iterations.

The first objective of this work was to quantitatively study the near-/far-field acoustic performance of the ducted propeller comparing to the open propeller counterpart, and it is concluded:

- 1) For the Grunwald case studied, the averaged acoustic strength is reduced due to the duct blockage by about 10 dB in the near-field and 5 to 10 dB in the far-field, while producing the similar amount of aerodynamic loads. The acoustic blockage effects of the duct are shown with details using the near- and far-field acoustic directivities. Especially, the fly-over noise calculations show that the ducted acoustic strength is about a quarter or in some cases half the magnitude of the un-ducted. A local acoustic valley is seen at the propeller disk passage due to the duct shielding. This feature may be exploited in flight path optimisation for minimised acoustics to communities.
- 2) The far-field acoustic performance of the optimised designs was also examined to check if the acoustic benefits are maintained after the aerodynamic optimisation. The far-field noise levels of the optimised designs remained almost the same as the original design and the acoustics was better than that of the open propeller counterpart. Particularly, the duct shape had a significant impact on the overall far-field acoustics. The duct shape optimisation and the coupled optimisation, where duct deformation was involved, altered both the far-field acoustic directivities

and the fly-by noise signal. With the reduced expansion ratios, the low far-field acoustic region was moved closer to the propeller disk. Signals of the blade twist optimisation were almost identical to that of the original without the duct deformation.

The second objective was to investigate the aerodynamic performance optimization by altering the duct and blade shapes upon adjoint methods, and it is concluded:

- 1) By altering the duct and blade shapes, the ducted propeller performance was effectively improved at  $\mu = 0.191$  by the proposed adjoint-based optimisation framework. Especially, the coupled duct/blade shape optimisation brought the greatest performance improvement comparing to the separate cases respectively for the duct and the blade. Compared to the original design, the coupled optimisation delivered higher performance at higher disk loadings/pitch settings. The performance was also improved at higher advance ratios but slightly penalised at lower advance ratios. The cross-wind performance of the duct shape optimisation, where largest duct deformation is observed, is shown only slightly penalised.
- 2) To improve the ducted propeller performance at high axial speeds, the sensitivity-driven optimisation decreased the duct inlet/outlet expansion ratio and reversed the original section camber. This deformation caused the duct to induce lower inflow velocity and flow rates through the propeller disk, thereby improving the inflow condition for the propeller and improving its thrust. For the blade shape, the global pitch was increased to accommodate the high inflow velocity. The blade twist optimisation increased the blade twist to offload the tip and to improve the efficiency. However, in the coupled optimisation, the blade twist was slightly eased. Regardless, combining with the duct deformation, the coupled optimisation offered the greatest performance improvement.

Future work will continue to explore the coupled duct/blade optimisation of the ducted propeller with multiple objectives at various operating conditions, with more design variables and larger design spaces. More investigations will also be made to further study the impact of the duct on the overall performance. Further, to pave the way for the future use of the ducted propeller, more complex problems need to be investigated numerically and experimentally, such as swirl recovery device or coaxial rotor design for improved performance, guide vanes or duct venting for vectorised thrust, structural/mechanical design etc.

## Acknowledgments

The sponsorship of the University of Glasgow and the China Scholarship Council is gratefully acknowledged.

## References

- [1] Filippone, A., and Barakos, G., “Rotorcraft systems for urban air mobility: A reality check,” *The Aeronautical Journal*, 2020, pp. 1–19.

- [2] Zhang, T., and Barakos, G. N., “High-fidelity CFD Validation and Assessment of Ducted Propellers for Aircraft Propulsion,” *Journal of American Helicopter Society*, 2020. doi:10.4050/JAHS.66.012008.
- [3] Zhang, T., and Barakos, G., “Review on Ducted Fans for Compound Rotorcraft,” *The Aeronautical Journal*, Vol. 124, No. 1277, 2020, pp. 941–974.
- [4] Yilmaz, S., Erdem, D., and Kavsaoğlu, M., “Effects of duct shape on a ducted propeller performance,” *51st AIAA Aerospace Sciences Meeting including the New Horizons Forum and Aerospace Exposition*, 2013, p. 803.
- [5] Carlton, J., *Marine propellers and propulsion*, Butterworth-Heinemann, 2018.
- [6] Gilbert, B., Oman, R., and Foreman, K., “Fluid dynamics of diffuser-augmented wind turbines,” *Journal of Energy*, Vol. 2, No. 6, 1978, pp. 368–374.
- [7] Grunwald, K. J., and Goodson, K. W., “Division of aerodynamic loads on a semispan tilting-ducted-propeller model in hovering and transition flight,” Tech. rep., NASA TN D-1257, 1962.
- [8] Grunwald, K. J., and Goodson, K. W., “Aerodynamic loads on an isolated shrouded-propeller configuration for angles of attack from -10 degrees to 110 degrees,” Tech. rep., NASA-TN-D-995, 1962.
- [9] Mort, K. W., and Gamse, B., “A wind-tunnel investigation of a 7-foot-diameter ducted propeller,” Tech. rep., NASA-TN-D-4142, 1967.
- [10] Hubbard, H. H., “Sound measurements for five shrouded propellers at static conditions,” Tech. rep., NACA-TN-2024, 1950.
- [11] Malgoezar, A. M., Vieira, A., Snellen, M., Simons, D. G., and Veldhuis, L. L., “Experimental characterization of noise radiation from a ducted propeller of an unmanned aerial vehicle,” *International Journal of Aeroacoustics*, 2019.
- [12] Kriebel, A. R., and Mendenhall, M. R., “Predicted and measured performance of two full-scale ducted propellers,” Tech. rep., NASA-CR-578, 1966.
- [13] Youngren, H., Drela, M., and Sanders, S., “Ducted Fan Design Code,” <http://web.mit.edu/drela/Public/web/dfdc/>, December 2005. Ducted Fan Design Code homepage, available on-line.
- [14] Drela, M., and Youngren, H., “Axisymmetric Analysis and Design of Ducted Rotors,” <http://web.mit.edu/drela/Public/web/dfdc/DFDCtheory12-31.pdf>, December 2005. Ducted Fan Design Code theory, available on-line.
- [15] Bontempo, R., and Manna, M., “Solution of the flow over a non-uniform heavily loaded ducted actuator disk,” *Journal of Fluid Mechanics*, Vol. 728, 2013, pp. 163–195.
- [16] Jimenez, B. G., and Singh, R., “Effect of duct-rotor aerodynamic interactions on blade design for hover and axial flight,” *53rd AIAA Aerospace Sciences Meeting*, 2015, p. 1030.

- [17] Biava, M., and Barakos, G. N., "Optimisation of ducted propellers for hybrid air vehicles using high-fidelity CFD," *The Aeronautical Journal*, Vol. 120, No. 1232, 2016, pp. 1632–1657.
- [18] Sheng, C., Zhao, Q., and Bi, N. P., "Numerical Investigations of Ducted Fan Hover Performance for FIW Applications," *53rd AIAA Aerospace Sciences Meeting*, 2015, p. 1935.
- [19] Rubio, R. C., Diaz, P. V., and Yoon, S., "High-Fidelity Computational Analysis of Ducted and Coaxial Rotors for Urban Air Mobility," *Proceedings of the 75th Annual Forum*, Philadelphia, 2019.
- [20] Schaller, D. F., "A technique for shape optimization of ducted fans," Master's thesis, Iowa State University, 2007.
- [21] Qing, J., Hu, Y., Wang, Y., Liu, Z., Fu, X., and Liu, W., "Kriging Assisted Integrated Rotor-Duct Optimization for Ducted Fan in Hover," *AIAA Scitech 2019 Forum*, 2019, p. 0007.
- [22] Ffowcs Williams, J. E., and Hawkings, D. L., "Sound generation by turbulence and surfaces in arbitrary motion," *Philosophical Transactions of the Royal Society of London. Series A, Mathematical and Physical Sciences*, Vol. 264, No. 1151, 1969, pp. 321–342.
- [23] Steijl, R., Barakos, G. N., and Badcock, K., "A framework for CFD analysis of helicopter rotors in hover and forward flight," *International Journal for Numerical Methods in Fluids*, Vol. 51, No. 8, 2006, pp. 819–847.
- [24] Biava, M., Woodgate, M., and Barakos, G. N., "Fully implicit discrete-adjoint methods for rotorcraft applications," *AIAA Journal*, Vol. 54, No. 2, 2015, pp. 735–749.
- [25] Antoniadis, A., Drikakis, D., Zhong, B., Barakos, G., Steijl, R., Biava, M., Vigevano, L., Brocklehurst, A., Boelens, O., Dietz, M., et al., "Assessment of CFD methods against experimental flow measurements for helicopter flows," *Aerospace Science and Technology*, Vol. 19, No. 1, 2012, pp. 86–100.
- [26] Steijl, R., and Barakos, G., "CFD analysis of complete helicopter configurations—lessons learnt from the GOAHEAD project," *Aerospace Science and Technology*, Vol. 19, No. 1, 2012, pp. 58–71.
- [27] Han, D., Pstrikakis, V., and Barakos, G. N., "Helicopter flight performance improvement by dynamic blade twist," *Aerospace Science and Technology*, Vol. 58, 2016, pp. 445–452.
- [28] Garcia, A. J., and Barakos, G. N., "Numerical simulations on the ERICA tiltrotor," *Aerospace Science and Technology*, Vol. 64, 2017, pp. 171–191.
- [29] Jarkowski, M., Woodgate, M., Barakos, G., and Rokicki, J., "Towards consistent hybrid overset mesh methods for rotorcraft CFD," *International Journal for Numerical Methods in Fluids*, Vol. 74, No. 8, 2014, pp. 543–576.
- [30] Menter, F., "Two-Equation Eddy-Viscosity Turbulence Models for Engineering Applications," *AIAA Journal*, Vol. 32, No. 8, 1993, pp. 1598–1605.

- [31] Mavriplis, D. J., “Discrete adjoint-based approach for optimization problems on three-dimensional unstructured meshes,” *AIAA journal*, Vol. 45, No. 4, 2007, pp. 741–750.
- [32] Shepard, D., “A two-dimensional interpolation function for irregularly-spaced data,” *Proceedings of the 1968 23rd ACM national conference*, 1968, pp. 517–524.
- [33] Higgins, R. J., Jimenez-Garcia, A., Barakos, G. N., and Bown, N., “High-fidelity computational fluid dynamics methods for the simulation of propeller stall flutter,” *AIAA Journal*, Vol. 57, No. 12, 2019, pp. 5281–5292.
- [34] Chirico, G., Barakos, G. N., and Bown, N., “Propeller installation effects on turboprop aircraft acoustics,” *Journal of Sound and Vibration*, Vol. 424, 2018, pp. 238 – 262.
- [35] Farassat, F., “Derivation of Formulations 1 and 1A of Farassat,” Tech. rep., NASA / TM-2007-214853, 2007.
- [36] Dighe, V. V., Avallone, F., and van Bussel, G., “Effects of yawed inflow on the aerodynamic and aeroacoustic performance of ducted wind turbines,” *Journal of Wind Engineering and Industrial Aerodynamics*, Vol. 201, 2020, p. 104174. doi: <https://doi.org/10.1016/j.jweia.2020.104174>.
- [37] Smith, D. A., Filippone, A., and Barakos, G. N., “Acoustic Analysis of Counter-Rotating Open Rotors with a Locked Blade Row,” *AIAA Journal*, 2020(available online). doi:10.2514/1.J059273.
- [38] Luo, B., Chu, W., and Zhang, H., “Tip leakage flow and aeroacoustics analysis of a low-speed axial fan,” *Aerospace Science and Technology*, 2020, p. 105700.
- [39] Kraft, D., “Algorithm 733: TOMP-Fortran Modules for Optimal Control Calculations,” *ACM Transactions on Mathematical Software*, Vol. 20, No. 3, 1994, pp. 262–281.
- [40] Johnson, S., “The NLOpt Nonlinear-Optimization Package,” <https://nlopt.readthedocs.io/en/latest/>, retived 3 Sep 2020.
- [41] Kulfan, B. M., “Universal parametric geometry representation method,” *Journal of aircraft*, Vol. 45, No. 1, 2008, pp. 142–158.
- [42] Roache, P. J., “Perspective: A Method for Uniform Reporting of Grid Refinement Studies,” *Journal of Fluids Engineering*, Vol. 116, No. 3, 1994, pp. 405–413.
- [43] Roache, P. J., “Verification of Codes and Calculations,” *AIAA Journal*, Vol. 36, No. 5, 1998, pp. 696–702.